Article

Developmental Cell

Self-organized pattern formation in the developing mouse neural tube by a temporal relay of BMP signaling

Graphical abstract

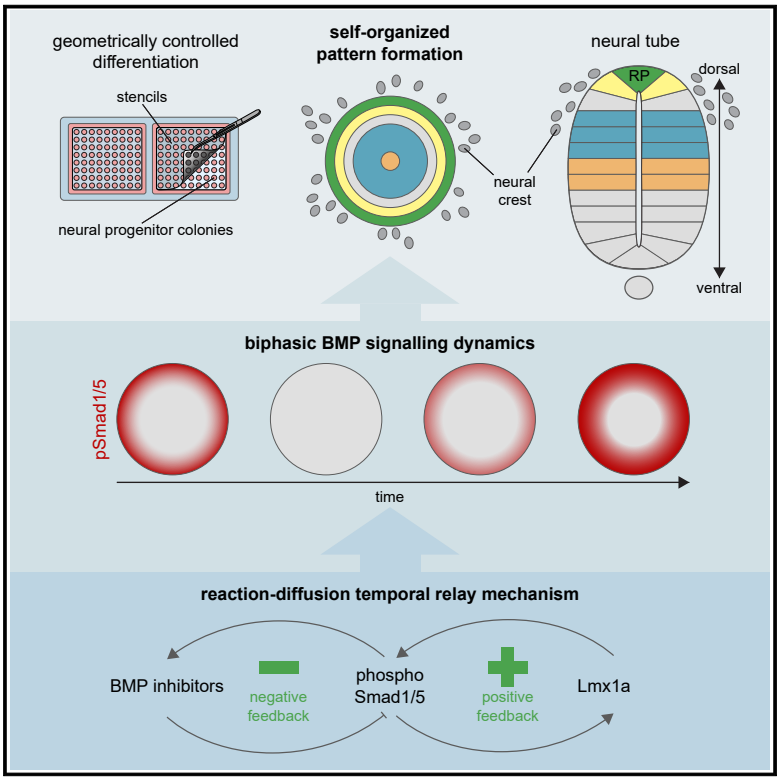

Highlights

- BMP drives self-organized patterning of dorsal neural tube progenitors
- Stencil-based system for 2D ESC differentiation allows for quantitative readout
- A temporal relay mechanism underlies sequential phases of BMP signaling
- Lmx1a links subnetworks of BMP signaling that operate at different timescales

Authors

Stefanie Lehr, David B. Brückner, Thomas George Minchington, Martina Greunz-Schindler, Jack Merrin, Edouard Hannezo, Anna Kicheva

Correspondence

edouard.hannezo@ist.ac.at (E.H.), anna.kicheva@ist.ac.at (A.K.)

In brief

Lehr and Brückner et al. develop an *in vitro* differentiation system that produces self-organized patterns of cell types similar to the ones observed in the dorsal neural tube. They find that to form these patterns, cells respond to sequential phases of BMP signaling, and they show how these phases are regulated.

Lehr et al., 2025, Developmental Cell *60*, 567–580
February 24, 2025
https://doi.org/10.1016/j.devcel.2024.10.024

CellPress

Developmental Cell

CellPress
OPEN ACCESS

Article

Self-organized pattern formation in the developing mouse neural tube by a temporal relay of BMP signaling

Stefanie Lehr,[1,2] David B. Brückner,[1,2] Thomas George Minchington,[1] Martina Greunz-Schindler,[1] Jack Merrin,[1] Edouard Hannezo,[1,*] and Anna Kicheva[1,3,*]

[1]Institute of Science and Technology Austria (ISTA), 3400 Klosterneuburg, Austria
[2]These authors contributed equally
[3]Lead contact
*Correspondence: edouard.hannezo@ist.ac.at (E.H.), anna.kicheva@ist.ac.at (A.K.)
https://doi.org/10.1016/j.devcel.2024.10.024

SUMMARY

Developing tissues interpret dynamic changes in morphogen activity to generate cell type diversity. To quantitatively study bone morphogenetic protein (BMP) signaling dynamics in the mouse neural tube, we developed an embryonic stem cell differentiation system tailored for growing tissues. Differentiating cells form striking self-organized patterns of dorsal neural tube cell types driven by sequential phases of BMP signaling that are observed both *in vitro* and *in vivo*. Data-driven biophysical modeling showed that these dynamics result from coupling fast negative feedback with slow positive regulation of signaling by the specification of an endogenous BMP source. Thus, in contrast to relays that propagate morphogen signaling in space, we identify a BMP signaling relay that operates in time. This mechanism allows for a rapid initial concentration-sensitive response that is robustly terminated, thereby regulating balanced sequential cell type generation. Our study provides an experimental and theoretical framework to understand how signaling dynamics are exploited in developing tissues.

INTRODUCTION

During development, several morphogens are reused in multiple tissues to control pattern formation and tissue growth. It is becoming increasingly clear that the temporal dynamics of morphogen signaling are relevant for pattern formation.[1–3] Multiple temporal features, such as duration of signaling or rate of change of signals over time, have been linked to downstream responses.[4–7] Nevertheless, in many systems, how the temporal dynamics of signaling are controlled and linked to cell fate decisions is unclear.

In the developing mouse spinal cord, pattern formation along the dorsal-ventral (DV) axis occurs in response to opposing bone morphogenetic protein (BMP) and sonic hedgehog (SHH) signaling gradients.[8] In the dorsal spinal cord, the acquisition of distinct neural progenitor identities has been proposed to depend on BMP levels, signaling duration or ligand type.[9–12] Yet, linking these dependencies to the dynamics of the BMP signaling gradient has been challenging. The spatiotemporal profile of BMP signaling in mouse has been measured in the closed neural tube,[13,14] but the earlier dynamics and the mechanisms that underlie the establishment of the gradient are poorly understood. BMP ligands are first expressed within the adjacent surface ectoderm, and later their expression is initiated within the dorsal-most cells of the neural tube, termed the roof plate (RP).[15,16] BMP ligands produced by both sources signal to the neural tube.

Besides the changing geometry of the BMP sources, the BMP signaling gradient in the neural tube forms concurrently with ongoing pattern formation and tissue growth, as well as morphogenetic changes resulting from neural crest (NC) development. Soon after their specification, the dorsally located NC progenitors undergo epithelial-to-mesenchymal transition and migrate out of the neural tube. The remaining progenitors give rise to spatially ordered domains consisting of RP, marked by LMX1A expression, and dorsal neural progenitor subtypes dp1–6 (Figure 1A).[17–19] How the dynamics of NC, RP, and neural progenitor specification interplay with the dynamics of the BMP signaling gradient remains unclear.

Here, we establish a two-dimensional (2D) *in vitro* system for mouse embryonic stem cell (ESC) differentiation with controlled geometry to study morphogen-driven pattern formation of the dorsal neural tube. This system uses stencils to achieve stereotyped geometry, and unlike other micropattern techniques,[20–22] it allows for tissue growth and cell migration. Our differentiation protocol yields reproducible self-organized patterns of dorsal neural tube cell types upon exposure to BMP. Strikingly, cells respond to a BMP signaling gradient that is activated in two sequential phases. We show that these biphasic dynamics result from a network of interconnected negative and positive

feedback loops that work on different timescales. Our analysis shows that the transcription factor LMX1A is a key mediator that relays the initial input to the formation of an endogenous BMP source. Our study identifies how the response to a morphogen self-generates complex spatiotemporal signaling dynamics that robustly encode cell diversity.

RESULTS

In vitro differentiated dorsal neural tube progenitors self-organize following a defined spatiotemporal sequence

Directed differentiation of ESCs provides a tractable system to investigate how cells interpret signals. Cells of the posterior neural tube (Figure 1A) arise from neuromesodermal progenitors (NMPs).[23,24] To generate these cell types *in vitro*, we based our approach on a monolayer protocol for generating mouse NMPs.[25] Sustained WNT activation in NMPs promotes paraxial mesoderm differentiation,[25] while BMP promotes lateral mesoderm identities.[26] By contrast, WNT signaling downregulation and treatment with retinoic acid (RA) promotes neural identities.[27] BMP4 is a dorsalizing factor in the developing neural tube,[15] hence we reasoned that exposure of NMPs to BMP4 in parallel with RA will generate dorsal neural tube progenitors (Figure 1B). Remarkably, we found that exposure of NMPs to 0.5 ng/mL BMP4 + RA did not result in the formation of a single cell type but in spatially patterned colonies expressing LMX1A at the periphery (Figure S1A). RNA sequencing (RNA-seq) analysis of differentiated colonies revealed that they express genes characteristic of NC, RP, and neural progenitor domains dp1–6 (Figure S1B). Expression of *Hox* paralogs 3–9 indicated that differentiated cells had posterior hindbrain, brachial and thoracic spinal cord axial identities (Figure S1C).

To quantitatively characterize these self-organized patterns, we optimized their reproducibility by introducing geometric constraints.[28] Culture on micropatterned surfaces is known to improve patterning reproducibility. However, it restricts colony growth to a predefined size. For our protocol, this led to the formation of irregular 3D structures containing clusters of NC cells (Figure S1D). To circumvent this, we established a protocol to initialize colonies on a defined geometry and to subsequently allow NC migration and colony expansion as a monolayer[29] (STAR Methods). To do this, cells were seeded on silicone stencils with circular through-holes 300 μm in diameter. After ∼20 h, before the CHIR pulse, stencils are removed (Figure 1B). This approach yields (2D) colonies in which all dorsal neural tube cell types are arranged in their correct spatial order, with migrating NC at the periphery and dorsal neural progenitors in the center (Figures 1C and 1D). The SOX2$^+$ neural progenitor core increases in size ∼5-fold over 96 h (Figures 1E and 1F).

To understand how this self-organized pattern forms, we analyzed the spatiotemporal profiles of gene expression. At the colony peripheries, we observed early migratory NC cells, marked by AP2ALPHA and SOX9 (Figures 1C and 1E), as early as 8 h after BMP4 exposure (Figures 1E and 1F). From 24 h onward, SOX10$^+$ late migratory NC cells were observed (Figures 1C and S1B). RP and dp1–6 genes formed nested concentric rings positioned from periphery to center, following the same spatial order as *in vivo* (Figures 1C–1E, S1G, and S1H). Analysis of the RP marker LMX1A showed that transcripts are first detectable after 12 h (Figures S1E and S1F) and protein after 24 h, while ATOH1$^+$ dp1 progenitors appeared at 72 h (Figures 1E and 1F). The temporal order of formation of these cell types is consistent with their formation *in vivo* (Figures S1G and S1H).

Biphasic dynamics of BMP signaling underlies self-organized cell fate patterning

The observed self-organization of cell fate patterns suggests the formation of a BMP signaling gradient in the cell colonies. To test this, we performed immunostaining against phosphorylated SMAD1/5 (pSMAD1/5), a direct readout of BMP signaling, at different time points of differentiation. This revealed that pSMAD1/5 has a graded profile with the highest levels at the colony periphery (Figures 2A and 2B). Surprisingly, pSMAD1/5 activation does not persist continuously over time but occurs in two distinct phases. Initially, a pSMAD1/5 gradient appears rapidly within 2 h of BMP addition (Figures 2A–2C). By 24 h, pSMAD1/5 activity declines to levels close to background. At 48 h, pSMAD1/5 is upregulated again in a graded manner from the margin, reaching maximum levels from 72 h onward (Figures 2A–2C). This raises the question of how such biphasic dynamics of BMP signaling are regulated and related to cell fate patterning.

To address this, we first asked whether the formation of a pSMAD1/5 gradient and organized cell fate pattern depends on the addition of exogenous BMP4. If no BMP is added to the medium, the formation of organized dorsal pattern did not occur. Instead, we observed sporadic non-patterned activation of pSMAD1/5 and LMX1A in a small fraction of colonies but no NC (Figures 3A and 3B).

To define critical time windows of BMP signaling for pattern formation, we used the BMP receptor inhibitor LDN193189 to inhibit signaling during defined time intervals. Inhibition of BMP signaling from t = 0 h for 24 h or longer severely impaired the formation of all dorsal cell types, including NC, RP, and dp1 (Figures 3C and 3D). Instead, an increasing fraction of neural progenitors adopted ventral (NKX6.1$^+$, OLIG2$^+$) identities (Figures 3C and 3D). BMP inhibition in the first 24 h also inhibited subsequent pSMAD1/5 signaling (Figure 3D). Thus, the first pSMAD1/5 phase is necessary for subsequent pSMAD1/5 signaling and the formation of self-organized cell fate pattern.

To understand whether the first phase of pSMAD1/5 is sufficient for pattern formation, we treated cells with BMP4 for 24 h and subsequently changed to medium that contained only RA. Strikingly, in this condition, pattern formation and the pSMAD1/5 profiles were similar to the case in which BMP exposure was continuous (Figures 3A, 3B, i and iii, S2A, and S2B). These observations suggested that cell fate patterning and pSMAD1/5 activity after the first 24 h are independent of exogenously added BMP, leading us to hypothesize that they depend on endogenous expression of BMP ligands.

To test this, we assessed the endogenous expression of BMP ligands using qPCR and hybridization chain reaction (HCR). The expression of several BMP-family ligands, including *Bmp6*, *Bmp7*, *Gdf7*, and *Bmp4*, begins at low levels at 24 h and continuously increases until 96 h (Figures S2C and S2D). Like pSMAD1/5 and LMX1A, *Bmp6* and *Gdf7* transcripts were

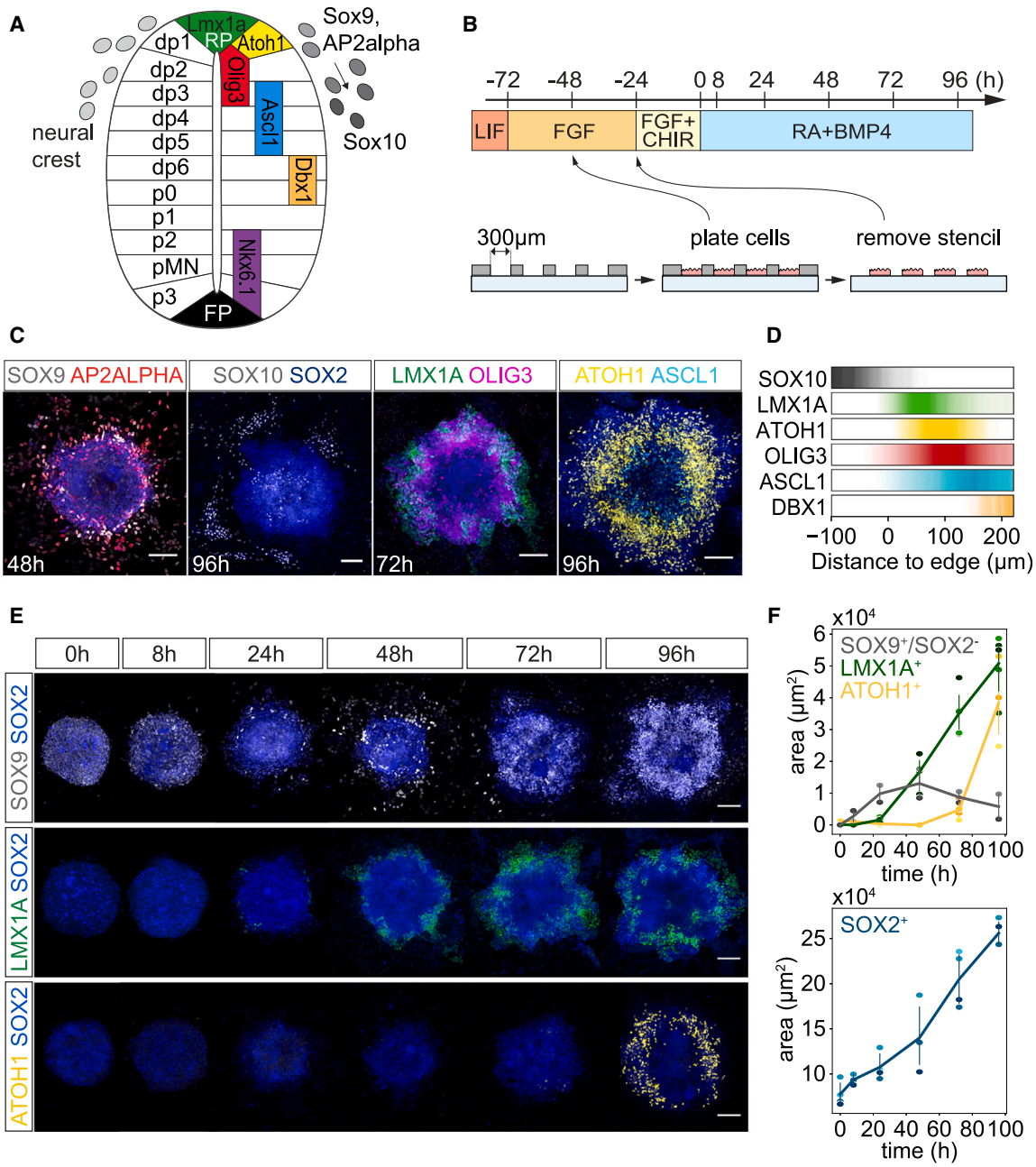

Figure 1. 2D stencil differentiation system captures dorsal neural tube patterning

(A) Gene expression pattern in the E10.5 neural tube. RP, roof plate; FP, floor plate.

(B) Differentiation protocol (top) and stencil method (bottom) used in this study. Throughout, t = 0 is the time when exogenous 0.5 ng/mL BMP4 is added.

(C and E) Immunostainings against the indicated markers show self-organized patterns. Scale bars, 100 µm.

(D) Quantifications of gene expression profiles from immunostainings at 96 h. Color intensity, mean FI. x axis denotes distance from colony edge, defined based on SOX2 expression, toward colony center (positive values), away from the colony (negative values). *n* = 23–38 colonies per gene.

(F) Mean expression area quantified from immunostainings. Dots, means of individual experiments; line, mean of all experiments. *n* = 26–79 (LMX1A), *n* = 8–64 (ATOH1), *n* = 12–21 (SOX9), and *n* = 25–52 (SOX2) colonies per gene per time point. Error bars, 95% CI.

localized at the colony periphery (Figure S2D). This is consistent with the possibility that these ligands induce the second phase of pSMAD1/5 activity. Consistent with this, inhibition of BMP signaling from 24 h onward using LDN prevents the activation of pSMAD1/5 during the second phase (Figures 3A and 3B, iv).

The inhibition of BMP signaling with LDN from 24, 48, or 72 h onward also resulted in a progressive decrease in LMX1A, SOX10, and ATOH1 expression (Figure S2E), suggesting that ongoing BMP signaling after the first 24 h is necessary for the correct expansion of these cell populations. Together, these results

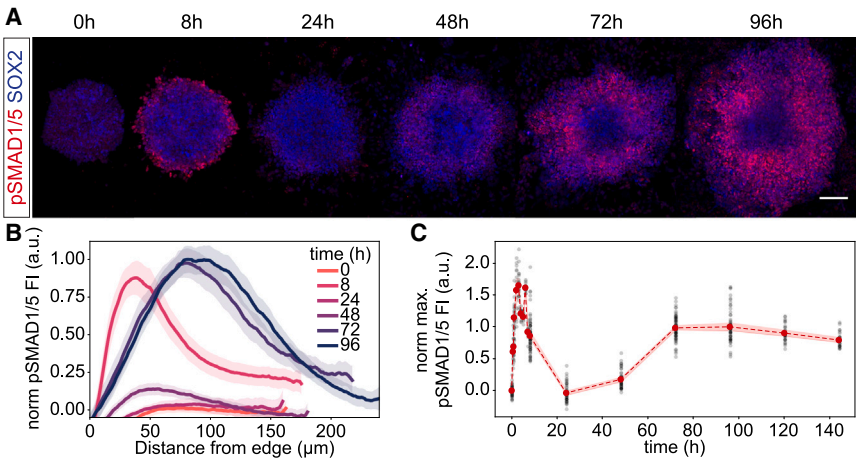

Figure 2. Biphasic temporal dynamics of pSMAD1/5 signaling

(A) pSMAD1/5 immunostaining of cells treated with 0.5 ng/mL BMP4. Scale bar, 100 μm.

(B) Mean spatial profiles of pSMAD1/5 fluorescence intensity (FI) at the indicated time points. Shaded regions, 95% confidence interval (CI). n = 36–51 colonies from 4 experiments.

(C) Maximum pSMAD1/5 FI of the spatial profiles was determined for each time point and plotted as a time course. Data show mean and 95% CI, sample sizes per time point: for t = 0.8–96 h, n = 54–92 (from 6 experiments); t = 0.5–7 h, n = 8–20 (from 2 experiments); t = 120 and 144 h, n = 30–31 (2 experiments).

indicate that the first peak of pSMAD1/5, which is dependent on exogenous BMP4, is necessary and sufficient to induce a second phase of pSMAD1/5 activity by inducing endogenous production of BMP ligands.

A temporal signaling relay underlies the biphasic dynamics of BMP signaling

To further investigate the mechanisms underlying pSMAD1/5 dynamics, we developed a spatiotemporal model of pSMAD1/5 signaling (STAR Methods). In our model, pSMAD1/5 levels depend on the local BMP concentration with constant sensitivity, except for cells at the colony edge, which are more sensitive to BMP (STAR Methods). Higher sensitivity to BMP at the edge has also been observed in other micropattern protocols.[22,30,31] In our case, this effect may be caused by BMP inhibitor diffusion away from the colony edge (Figures S3A and S3B; STAR Methods). pSMAD1/5 induces the expression of BMP ligands, consistent with the experimental data (Figures S2C and S2D). The downregulation of pSMAD1/5 at 24 h and the observation that exogenous signaling is not required to maintain pSMAD1/5 levels after 24 h (Figures 3A, 3B, and S2B) imply that a negative regulator is also relevant to the dynamics. The RNA-seq dataset indicated that several BMP inhibitors are upregulated in response to BMP as early as 8 h (Figure S3C), consistent with previous findings that BMP inhibitors are also often targets of the pathway.[32,33] We therefore included in the model a generic inhibitor of BMP, which is produced by pSMAD1/5 activity and inhibits BMP-mediated pSMAD1/5 activation (Figure 4A).

Numerical simulations indicated that this minimal circuit (Figure 4A) produces a pSMAD1/5 gradient from the margin to the center of colonies (STAR Methods) with an amplitude that overshoots before reaching steady-state levels at long times (Figures 4B, S4, and S5). In the model, the pSMAD1/5 gradient decays with near-constant length scale over time. Hence, the temporal dynamics of the maximum pSMAD1/5 levels are qualitatively independent of the spatial profile. Thus, in order to focus on the temporal dynamics of the circuit, we plot the maximum levels of pSMAD1/5 signaling at every time point (Figure 4B) and use this representation in subsequent analysis. Altogether, these simulations show that this simple negative feedback circuit qualitatively recapitulates the first phase of the pSMAD1/5 dynamics (Figures 2C and 4B).

We then asked if this circuit alone could explain how pSMAD1/5 is upregulated in phase two. Analysis of the model dynamics as a function of parameters and initial conditions showed that pSMAD1/5 levels relax to either zero or non-zero steady-state level (Figures 4C and S4B–S4H; STAR Methods). The downregulation of pSMAD1/5 from its maximum to its steady-state value differed across this parameter space (Figure 4C). This allowed us to constrain the model parameters to the non-zero steady-state regime and to determine that the initial exogenous BMP4 concentration of 0.5 ng/mL is above the steady-state BMP level (Figure 4C; STAR Methods). Notably, this simple circuit does not predict a second large amplitude pulse of pSMAD1/5 activity in any parameter regime (Figure S4). This indicates that the minimum model (Figure 4A) cannot explain the upregulation of pSMAD1/5 in phase two.

Instead, the observation that BMP signaling in the initial phase is required for signaling in the second phase (Figures 3C and 3D) suggested the presence of positive feedback on BMP acting at slower timescales compared with phase one. We hypothesized that such positive feedback could be mediated via the formation of RP cells, which are a known source of BMP ligands *in vivo*.[11] LMX1A is an essential regulator of RP formation *in vivo*[34] and a BMP target gene.[11] Therefore, we included it as a candidate mediator of the positive feedback (Figure S6; STAR Methods).

If LMX1A is required to upregulate pSMAD1/5 in phase two, our model predicts that the absence of LMX1A should significantly reduce, but not completely abolish, pSMAD1/5 signaling at long times, while leaving the short timescale dynamics unchanged (Figures 4B and S4; STAR Methods). To test this, we generated *Lmx1a* knockout (KO) cells using CRISPR-Cas9 and verified that these cells generate NMPs with similar efficiency as wild-type cells (Figure S7A). In the *Lmx1a* KO cells, the pSMAD1/5 levels were similar to those of control until 24 h but were downregulated at later time points (Figures 4D and 4I). Furthermore, the expression of endogenous *Bmp6*, *Bmp7*, and *Gdf7* was strongly reduced in *Lmx1a* KO cells, compared with control, at 96 h (Figure S7B). This suggests that the second phase of BMP signaling depends on the induction of BMP ligand

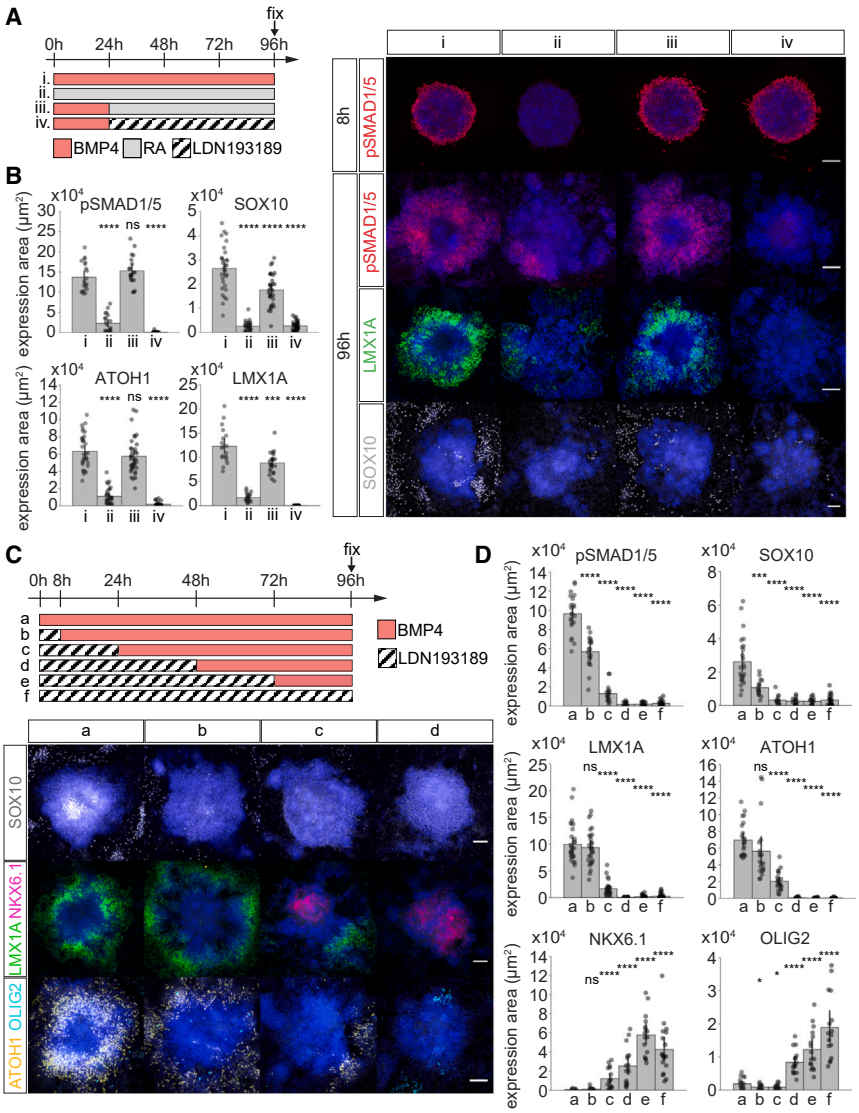

Figure 3. Time window perturbations define the temporal requirements for BMP signaling

(A) Schematic of differentiation conditions (left). RA + 0.5 ng/mL BMP4 (red), RA (gray), RA + 1 μM LDN193189 (hatched). Cells were harvested at 96 h. Immunostainings for the indicated markers and SOX2 (blue) (right). Scale bars, 100 μm.

(B) Quantification of the positive area of the experiment in (A). For SOX10 in (B) and (D), the SOX10^{+}, Sox2^{-} area was quantified. n = 19–36 per condition. Conditions ii–iv were compared with i with two-tailed t test: ns $p > 0.05$, *$p \leq 0.05$, **$p \leq 0.01$, ***$p \leq 0.001$, ****$p \leq 0.0001$.

(C) Differentiation conditions, colors as in (A). Cells were harvested at 96 h. Representative images (bottom) at 96 h. SOX2 in blue. Occasional OLIG2^{+} cells in condition a are SOX2 negative and located at the periphery. Scale bars, 100 μm.

(D) Quantification of positive area of the experiment in (C). n = 13–25 (SOX10), n = 26–31 (LMX1A), n = 20–24 (ATOH1), n = 14–22 (pSMAD1/5), n = 16–18 (NKX6.1), and n = 16–19 (OLIG2). Conditions b–f were compared to condition a with t test as in (B).

expression by LMX1A, consistent with the *Lmx1a* mutant phenotype *in vivo*.[35]

Our results indicate that LMX1A positively regulates pSMAD1/5 activity via the induction of BMP ligands and is induced by pSMAD1/5 forming a positive feedback loop. The simplest linear implementation of these interactions in the model (Figure S6A) showed that to produce well-defined phases, the characteristic timescale of LMX1A activity had to be >∼20 h (STAR Methods). To further constrain the model parameters, we measured the actual degradation timescales. The decay of pSMAD1/5 levels in colonies where BMP signaling was abruptly inhibited at t = 72 h, using a high concentration (3 μM) of LDN193189 (Figure 4E), revealed a half-life for pSMAD1/5 of 0.43 ± 0.03 h, consistent with previous observations.[36] Inhibition of BMP signaling with LDN also caused LMX1A levels to decline over time (Figure S7C), consistent with a requirement for pSMAD1/5 signaling for *Lmx1a* expression. Nevertheless, to obtain a direct estimate of the LMX1A degradation rate that does not rely on assumptions about its link to pSMAD1/5, we inhibited protein production using cycloheximide (Figure 4F). This indicated that the half-life of LMX1A corresponds to 4.7 ± 0.5 h. This measured half-life was inconsistent with the predictions of the simple model in which LMX1A activation occurs by pSMAD1/5 alone (Figures S6A and S6B; STAR Methods), suggesting that the positive feedback loop involves additional non-linear interactions. Using the measured timescales of pSMAD1/5 and LMX1A degradation, we found that the experimentally observed dynamics are captured by a model in which LMX1A is weakly activated by pSMAD1/5 but beyond a threshold reinforces its expression in a pSMAD1/5-dependent manner (Figure S6C). Therefore, we set out to investigate how the LMX1A positive feedback occurs.

WNT signaling promotes the second phase of BMP activity by positive feedback on LMX1A

Besides BMP ligands, the RP *in vivo* also expresses *Wnt1*, *Wnt3*, and *Wnt3a*,[37] and *Wnt1* expression is influenced by BMP signaling.[38] Hence, we hypothesized that WNT signaling is involved in a positive feedback loop with LMX1A (Figure 4G). Several WNT ligands were expressed in our default conditions (Figure S8A). *Wnt1* was expressed within the *Lmx1a* domain from 48 h onward, consistent with its induction by LMX1A (Figures S8B and S8C). To assess the WNT signaling activity, we measured the mRNA levels of the WNT target gene *Axin2*.[39] *Axin2* levels were high at t = 0 h as a result of the preceding CHIR pulse and decayed to background levels within 24 h, indicating a half-life for WNT signaling of 5.6 ± 2.1 h (Figure S8D). From 48 h onward, *Axin2* was expressed in the domain of *Lmx1a* activation in the periphery of colonies (Figure S8B). Further

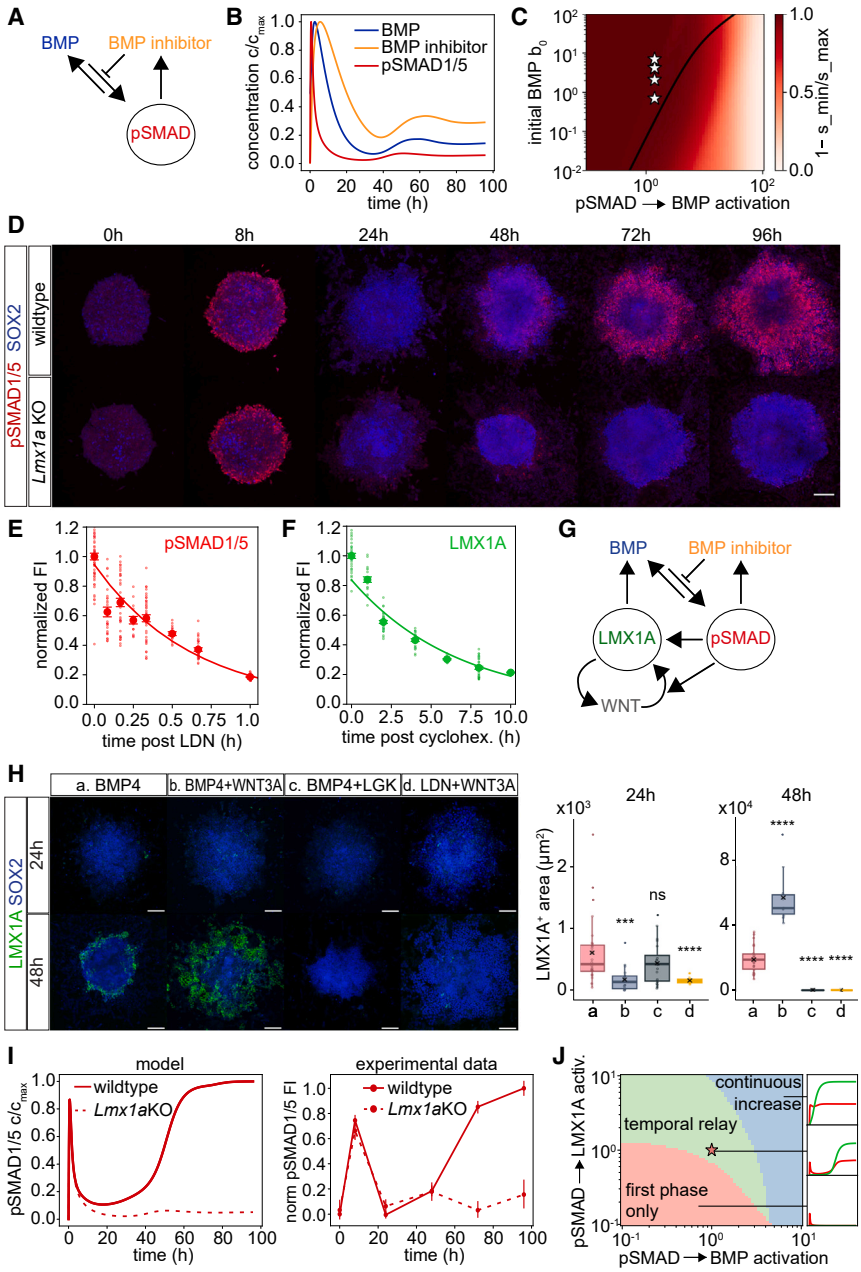

Figure 4. Regulatory network underlying the BMP signaling dynamics

(A and B) Minimal interaction network (A) captures the first-phase signaling dynamics (B).

(C) Downregulation strength (color-coded, s_max is max pSMAD level in the time course and s_min the subsequent minimum), b_0 initial BMP concentration, $a_b^{(s)}$ activation strength of BMP by pSMAD1/5.

(D) pSMAD1/5 immunostaining in cells treated with 0.5 ng/mL BMP4. Scale bar, 100 µm.

(E) pSMAD1/5 FI (points) upon treatment with 3 µM LDN193189 from t = 72 h. n = 15–60 per time point. Error bars, SEM. Exponential fit (line).

(F) LMX1A FI (points) upon treatment with 10 µM cycloheximide from t = 72 h. n = 10–35 per time point. Error bars, SEM. Exponential fit (line).

(G) Extended network including pSMAD-dependent positive feedback via LMX1A and WNT.

(H) LMX1A immunostaining in cells treated with 0.5 ng/mL BMP4 (a), 0.5 ng/mL BMP4 + 1 µg/mL WNT3A (b), 0.5 ng/mL BMP4 + 5 µM LGK974 (c), or 300 nM LDN + 1 µg/mL WNT3A (d) and quantification. Two-tailed t test: ns $p > 0.5$, ***$p \leq 0.001$, ****$p \leq 0.0001$. Scale bar, 100 µm. n = 10–20 per condition.

(I) Simulation of the model in (G) (left). *Lmx1a* KO (dashed) is simulated by removing all LMX1A production terms. Quantification of the experiment in (D) (right). Error bars, 95% CI. n = 52–83 per time point (wild type), n = 10–25 (*Lmx1a* KO).

(J) Types of pSMAD1/5 (red) and LMX1A (green) behaviors (right) as a function of $a_b^{(s)}$ and $a_l^{(s)}$. Star, parameters used in the model. Details in STAR Methods.

supporting the role of LMX1A in inducing WNT ligand expression, we found that *Wnt1*, *Wnt3*, and *Wnt3a* are downregulated in *Lmx1a* KO cells (Figure S8E).

These data support the positive regulation of WNT signaling by LMX1A, but does LMX1A expression depend on WNT signaling? To test this, we inhibited WNT signaling using LGK974, which blocks WNT ligand secretion (Figure 4H). In this condition, LMX1A expression was unchanged at 24 h and absent at 48 h, suggesting that WNT signaling does not contribute to the initial expression of LMX1A but is required for its maintenance and strongly contributes to its expansion (Figure 4H). Consistent with this, simultaneous inhibition of BMP signaling and treatment with WNT3A showed that WNT signaling alone is not sufficient to induce LMX1A expression (Figure 4H). Treating the cells with WNT3A without BMP inhibition induced disordered LMX1A activation (Figure S8F), reminiscent of the RA-only condition (Figure 3A), while in the presence of BMP, WNT3A led to an expansion of the LMX1A domain (Figure 4H).

Together, these results support a model whereby LMX1A expression is amplified through a positive feedback loop that involves both BMP and WNT signaling (Figures 4G, S6D, and S9; STAR Methods). LMX1A expression is initiated via weak activation by pSMAD1/5. Upon reaching a threshold, LMX1A enters a WNT- and pSMAD1/5-dependent positive feedback loop that amplifies its expression in the second phase (STAR Methods). Crucially, this model captures the experimentally observed time course of pSMAD1/5 signaling in wild-type and *Lmx1a* KO cells (Figures 4I and 4J), as well as the measured half-lives of pSMAD1/5, LMX1A, and WNT signaling activity. A key prediction of this model is that expression of LMX1A on its own can trigger the positive feedback loop, leading to upregulation of BMP signaling. To test this, we overexpressed LMX1A using a doxycycline-inducible promoter. Consistent with our prediction, we found that overexpression of LMX1A increased the pSMAD1/5 levels of BMP4-treated cells (Figures S7D and S7E; STAR Methods). Crucially, we found that in the absence of

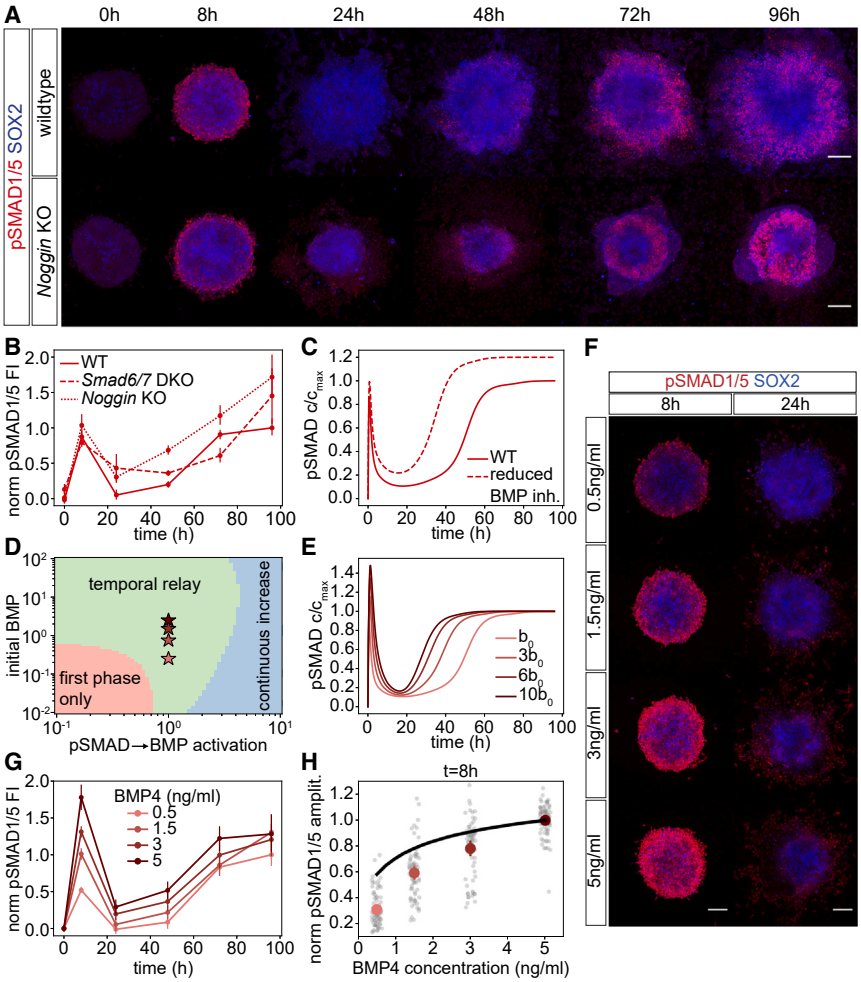

Figure 5. Signaling dynamics in BMP inhibitor knockouts and different concentrations of BMP4

(A) pSMAD1/5 immunostaining in cells treated with 0.5 ng/mL BMP4. Scale bar, 100 μm.

(B) Mean and 95% CI pSMAD1/5 FI in immunostainings. Images per time point from >2 experiments: n = 59–91 (wild type [WT]), n = 23–39 (*Nog* KO), n = 12–18 (*Smad6/7* DKO).

(C) pSMAD1/5 dynamics in control (solid) vs. *Nog* KO (dashed) simulated by reducing the activation rate of BMP inhibitor by 30%.

(D) Phase diagram of model behaviors (illustrated in Figure 4J) as a function of $a_b^{(s)}$ and b_0. Stars, parameters corresponding to tested concentrations.

(E) Simulations of pSMAD1/5 dynamics for 1, 3, 6, and 10 times the initial BMP concentration (b_0).

(F) pSMAD1/5 and SOX2 immunostaining of cells treated with indicated BMP4 concentrations. Scale bar, 100 μm.

(G) Mean with 95% CI pSMAD1/5 FI in immunostainings. FI normalized to the max FI in the 0.5 ng/mL BMP4 condition (STAR Methods). n = 18–76 per time point and concentration.

(H) Predicted (line) and measured (dots) pSMAD1/5 level at 8 h. Error bars, 95% CI. n = 70–76 per condition from 4 experiments.

exogenous BMP4, LMX1A-overexpressing cells promoted endogenous LMX1A expression in a non-cell-autonomous manner (Figure S7F), which is consistent with the positive feedback on LMX1A via diffusible ligands implemented in the model.

Altogether, our analysis suggests that the two phases of pSMAD1/5 signaling arise due to a timescale separation between two interacting subnetworks: a rapid first phase driven by negative feedback on BMP by the induction of BMP inhibitors and a slow second phase driven by positive feedback that involves the transcription factor LMX1A and its interaction with WNT signaling. The signal is relayed over time from the fast to the slow subnetwork.

The initial signaling response is BMP concentration sensitive but with a robust duration

Our model makes several testable predictions. First, it predicts that BMP inhibitors that temporally restrict the first phase are produced in a BMP-dependent manner (STAR Methods). RNA-seq and HCR analyses indicated that BMP4 treatment rapidly induces the expression of a subset of several BMP inhibitors, including *Noggin*, *Smad6*, and *Smad7* (Figures S3C and S3D). Inhibitor induction occurs in a BMP4 concentration-dependent manner, consistent with our model (Figure S3C). The expression of these BMP inhibitors was further maintained at 24 h as pSMAD1/5 levels are downregulated (Figure S3C), suggesting that they are plausible mediators of the pSMAD1/5 dynamics in this system.

We further used CRISPR-Cas9-mediated genome editing to generate KO ESC lines for these inhibitors (Figure S7A; STAR Methods). Analysis of *Nog* KO cells revealed that pSMAD1/5 levels at 8 h were similar to wild-type cells; however, the subsequent downregulation occurred less efficiently in the KO, resulting in higher pSMAD1/5 levels from 24 h onward (Figures 5A and 5B). Similar results were obtained in cells with a double KO (DKO) of *Smad6* and *Smad7* (*Smad6/7* DKO) (Figures 5B and S10A). This phenotype is captured by our model with reduced production of BMP inhibitor (Figure 5C). Together, these results suggest that the duration of the initial pSMAD1/5 signaling phase depends on the pSMAD1/5-dependent expression of several BMP inhibitors.

Another model prediction is that the biphasic dynamics are observed across a range of initial BMP concentrations, b_0, which represents the exogenous BMP added to the culture media (Figures 5D and S11A; STAR Methods). Furthermore, the amplitude of the first-phase peak increases with increasing BMP concentration (Figures 5E, S11A, and S11B). Consistent with this, the maximum level of pSMAD1/5 at 8 h increases with the exogenous concentration of BMP4 in close agreement with the model (Figures 5F–5H and S10B). Moreover, upon downregulation, pSMAD1/5 reaches minimum levels that correlate with the initial concentration. Yet, the time of the downregulation is robust to the concentration of BMP in both the model and experimental data (Figures 5F, S10C, S11C, and S11D). This shows that the duration of the first signaling phase is independent of the exogenous BMP concentration. Our model further indicates that in

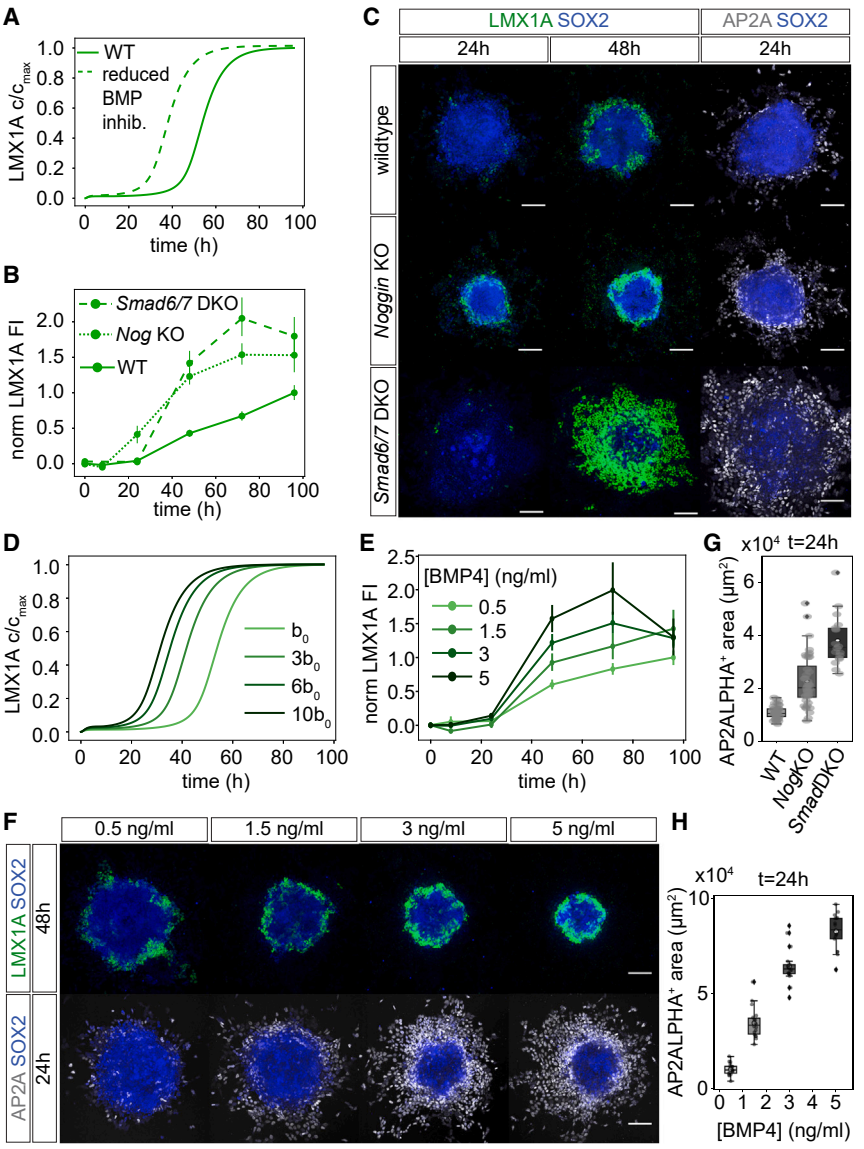

Figure 6. LMX1A and NC dynamics upon perturbations in BMP signaling

(A) Simulation of LMX1A levels for WT (solid) and 30% reduced BMP inhibitor activation rate (dashed).

(B) Mean and 95% CI of maximum LMX1A FI from immunostainings. Images per time point: n = 7–49 (WT), n = 8–34 (*Nog* KO), and n = 8–26 (*Smad6/7* DKO).

(C) Immunostainings in WT, *Nog* KO, and *Smad6/7* DKO cells. Scale bars, 100 μm.

(D) Simulations of LMX1A dynamics for 1, 3, 6, and 10 times the initial BMP concentration.

(E) Quantification of LMX1A (as in B) for cells cultured at the indicated BMP4 concentrations. n = 5–30 per data point.

(F) Immunostained cells treated with indicated BMP4 concentrations. Scale bar, 100 μm.

(G) Quantification of AP2ALPHA$^+$ area at 24 h. n = 43 (WT), n = 40 (*Nog* KO), and n = 18 (*Smad6/7* DKO).

(H) AP2ALPHA$^+$ area at 24 h correlates with BMP4 concentration. n = 17–18 per concentration. G, H: Box, median and IQR; white circle, mean.

See also Video S1.

contrast to the first phase, the maximum levels reached at long times are independent of the initial BMP concentration (Figure 5E). Nevertheless, the timescale of the approach to steady state is faster for higher concentrations, which is consistent with the differences observed in the discrete time points (between 48 and 72 h) sampled in our data (Figure 5H).

Altogether, our analysis shows that the initial-peak pSMAD1/5 amplitude provides a rapid and sensitive readout of the exogenous BMP concentration, whereas the underlying negative feedback mechanism via the BMP inhibitors ensures the robust termination of the first phase of pSMAD1/5 signaling. Finally, the second phase converges to a concentration-independent pSMAD1/5 signaling level, which depends on LMX1A.

The biphasic BMP signaling dynamics influence pattern formation via LMX1A

How do the dynamics of BMP signaling influence downstream pattern formation? To address this, we first asked how reduced BMP inhibitor production affects LMX1A expression. The model predicts that this will lead to an earlier increase and higher levels of LMX1A (Figures 6A and S12). Consistent with this, LMX1A is upregulated and observed earlier in *Nog* KO cells (Figures 6B and 6C). Similarly, *Smad6/7* DKO cells have increased LMX1A levels from 48 h onward (Figures 6B and 6C). These results suggest that the efficient downregulation of pSMAD1/5 after the first phase affects LMX1A dynamics and limits LMX1A expression.

Our results imply that LMX1A expression is dependent on the first BMP signaling phase. Like pSMAD1/5 (Figures 5F–5H), the pre-steady-state levels of LMX1A are predicted to be dependent on the initial BMP4 concentration (Figures 6D and S12D–S12F). The experiments confirm this prediction: LMX1A levels increase with BMP4 concentration prior to 96 h (Figures 6E and 6F). Consistent with the concentration-independent steady state predicted by the model, the LMX1A levels observed at the last time point in our time course (96 h) converge to a common state (Figure 6E).

The initial phase of BMP signaling is also critical for the specification of NC. AP2ALPHA and SOX9 expression are first detected at low levels at 8 h, and migrating NC is visible at 24 h (Figures 1E and 1F). To determine the initial location of NC cells, we generated mScarlet-I-NLS reporter cells (STAR Methods). Time-lapse imaging of differentiating colonies over 16 h at different BMP4 concentrations, together with AP2ALPHA immunostaining at the end time point, confirmed that NC cells initially localized at the colony edge migrate away from it over time (Figures S10D and S10E; Video S1). Like LMX1A, the number

of AP2ALPHA$^+$ NC cells is significantly increased after 24 h in *Nog* KO and *Smad6/7* DKO cells (Figures 6C and 6G). Furthermore, the amount of AP2ALPHA$^+$ cells at 24 h increases with BMP4 concentration and the pSMAD1/5 amplitude at 8 h (Figures 6F and 6H). NC cells lose SOX2 expression as they undergo epithelial-to-mesenchymal transition and migrate out of the colony, which results in smaller SOX2$^+$ colonies at higher exogenous BMP4 concentrations (Figure 6F). Overall, similar to LMX1A, these observations indicate that pSMAD1/5 levels, starting from the initial phase, as well as the duration of signaling, affect the amount of NC.

To exclude that the observed changes in LMX1A dynamics are an indirect consequence of NC specification, we inspected LMX1A domain formation in *Sox9* KO cells (STAR Methods). *Sox9* mutant mouse embryos have defects in neural stem cell maintenance[40] and lack functional NC due to a survival defect.[41] Consistent with the mouse phenotype, NC cells are markedly reduced in the *Sox9* KO (Figure S13A). Nevertheless, the onset of LMX1A expression and the fraction of LMX1A$^+$ SOX2 progenitors in *Sox9* KO are similar to control (Figures 7A and 7B). This is consistent with previous qualitative observations of *Sox9*$^{-/-}$ embryos[41] and suggests that the NC does not affect the specification of RP fate.

To assess the effects of the second signaling phase, we inspected pattern formation in *Lmx1a* KO cells. The formation of the dp1 domain, characterized by ATOH1 expression, was impaired in the *Lmx1a* KO (Figure S13B), consistent with the *in vivo* phenotype of mutants that lack RP.[42] Surprisingly, at 24 h, *Lmx1a* KO colonies had increased levels of AP2ALPHA cells (Figures 7C and 7D), suggesting that LMX1A inhibits NC specification at early stages. At 72 and 96 h, neither AP2ALPHA nor SOX9$^+$ NC cells could be observed outside the SOX2$^+$ core of the colony in *Lmx1a* KO cells, indicating that LMX1A is required for the normal maturation of NC, either directly or indirectly via signals produced by LMX1A$^+$ cells. Thus, the phenotype of *Lmx1a* KO cells suggests that LMX1A performs a dual role, i.e., to inhibit early NC specification and to promote NC maturation and migration. Altogether, our findings indicate that the amplitude and duration of the early signaling phase are critical for the correct balance between NC, LMX1A, and neural progenitor domains. In turn, the second signaling phase is required for the maturation and maintenance of NC, RP expansion, and specification of neural progenitor subtypes.

Biphasic BMP signaling dynamics underlie pattern formation *in vivo*

The biphasic BMP signaling dynamics *in vitro* led us to investigate the BMP dynamics in mouse embryos. As embryos undergo posterior extension over time, cells shift their positions away from the posterior tip yet retain their approximate anterior-posterior (AP) positions relative to each other,[43,44] suggesting that the spatial profiles of gene expression and signaling along the AP axis represent approximately the temporal changes experienced by cells. Therefore, we quantified the levels of pSMAD1/5 along the AP axis of E8.5 embryos, focusing on the neural plate border region, which most closely corresponds to the edge of *in vitro* generated colonies (Figures 7E and 7F). Notably, we observed that along the border of the caudal neural plate, pSMAD1/5 levels are not uniform but are high within and posterior to the caudolateral epiblast region where NMPs reside, low around the middle, and increase again in the anterior caudal neural plate (Figures 7E and 7F). Similar to the *in vitro* culture, we detected *Noggin* transcripts in the region where pSMAD1/5 levels were low (Figures 7E and 7F). In addition, *Lmx1a* expression was detected in the anterior caudal neural plate, at AP positions that coincided with increased pSMAD1/5 levels (Figures 7E and 7F). These observations suggest that similar to the *in vitro* situation, the levels of pSMAD1/5 experienced by cells at the neural plate border undergo biphasic dynamics.

To test whether BMP signaling dynamics affect pattern formation *in vivo*, we analyzed the effects of genetic deletions of BMP inhibitors on LMX1A at different time points. Our model predicts that early deletion of BMP inhibitors will lead to increased pSMAD1/5 and LMX1A expression, while later deletions will have a lesser effect (Figure S13C; STAR Methods). To test this, we conditionally deleted *Noggin* in mouse embryos, using a floxed allele crossed to two different Cre lines (Figures S13D and S13E; STAR Methods). In the first case, *Nog* was knocked out in SOX2$^+$ cells using tamoxifen-inducible Sox2-CreERT2 induced at E6.5. At E10.5, these embryos had larger LMX1A$^+$ RPs compared with controls (Figure S13D), consistent with the *in vitro* observations in *Nog* KO cells (Figures 6B and 6C). In the second case, *Nog* was specifically deleted in *Wnt1*-expressing cells using Wnt1-Cre. The endogenous expression of *Wnt1* is initiated in the closed neural tube (Figure S13F); hence, this represents a later deletion of *Nog*. In contrast to the early deletion, the RP size in Wnt1-Cre::*Nog*$^{Flox/Flox}$ mutants was similar to control littermates (Figure S13E).

Altogether, these results indicate that pSMAD1/5 levels are temporally regulated in the neural plate by *Noggin* prior to the endogenous expression of *Wnt1*, which marks the second phase of BMP signaling. The downregulation of pSMAD1/5 in the neural plate border restricts the duration of pSMAD1/5 signaling and thereby influences the size of the LMX1A domain. Altogether, our findings reveal how RP formation and dorsoventral patterning of the closed neural tube depend on earlier BMP signaling that occurs as cells leave the caudolateral epiblast.

DISCUSSION

Signaling relays have long been considered as possible mechanisms of morphogen gradient formation.[45] In these mechanisms, morphogens that spread at short range expand their activity range by inducing ligand production in adjacent cells. An example of this is NODAL signaling during zebrafish and human gastrulation.[46,47] Relay mechanisms that can give rise to millimeter-long gradient ranges, such as the WNT signaling gradient in planaria, have also been described.[48] Here, we uncovered a relay mechanism that intrinsically operates over time, rather than in space, creating sequential induction of morphogen ligand production and thereby signaling phases. This enables morphogen reuse within a tissue for different purposes, i.e., first to rapidly specify the neural plate border in a concentration-sensitive manner and then to reform the gradient and use it to specify the fates of dorsal neural progenitor subtypes along the DV axis.

The mechanisms that contribute to dynamic changes in signaling can be difficult to manipulate and disentangle *in vivo*

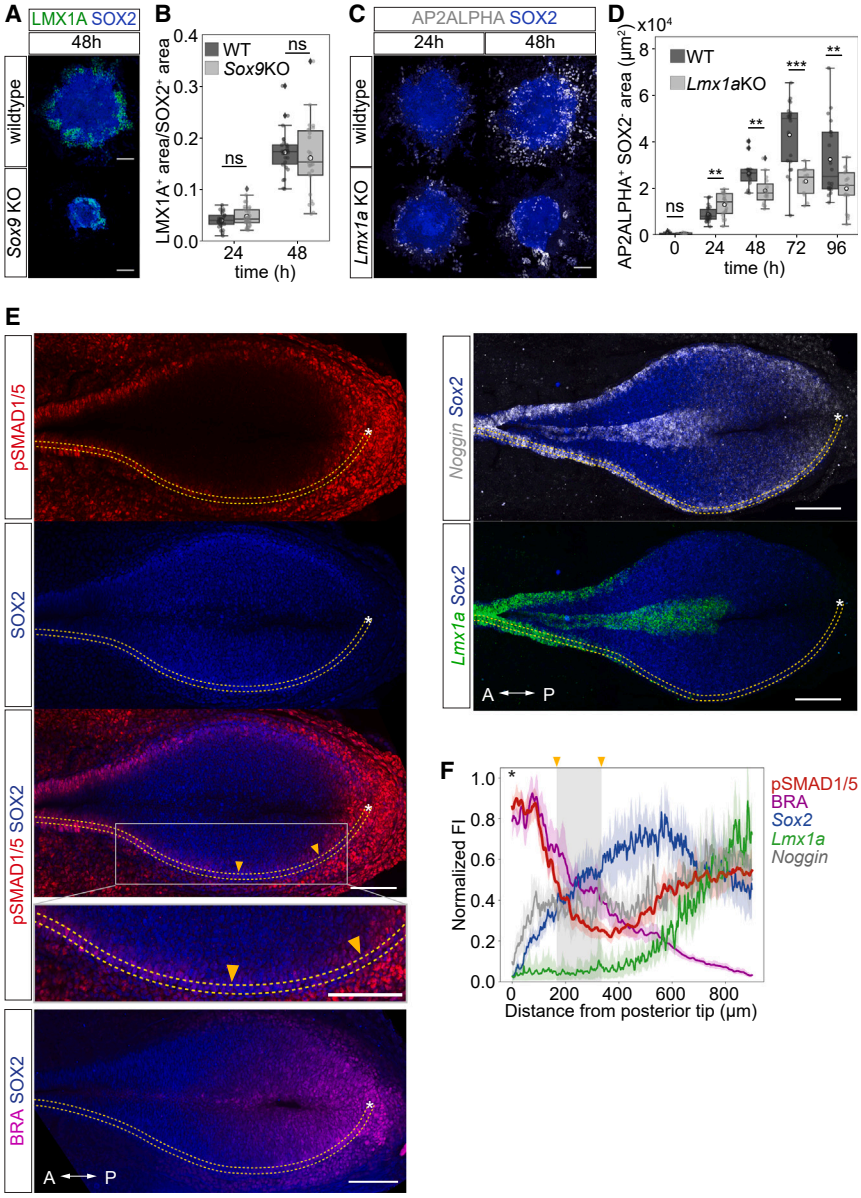

Figure 7. pSMAD1/5 signaling dynamics in the mouse spinal cord at E8.5

(A) WT and *Sox9* KO cells immunostained for LMX1A. Scale bar, 100 μm.

(B) Similar LMX1A$^+$ relative to SOX2$^+$ area in WT and *Sox9* KO cells. $n = 25–26$ (WT), $n = 26–31$ (*Sox9* KO) per time point. Two-tailed t test: ns $p \geq 0.05$. In (B) and (D): box, median and IQR; white circle, mean.

(C) AP2ALPHA immunostaining.

(D) Quantification of AP2ALPHA$^+$ SOX2$^-$ area. $n = 8–22$ (WT) and $n = 8–20$ (*Lmx1a* KO). Two-tailed t test: $^{**}p \leq 0.01$, $^{***}p \leq 0.001$.

(E) Neural plate of E8.5 mouse embryos. Maximum FI projections of pSMAD1/5, SOX2, and T/BRA immunostainings (left) and *Noggin*, *Lmx1a*, and *Sox2* HCR (right). Anterior, left. Region of interest (ROI) used for quantification (yellow dashed outline). Arrowheads delimit approximate position of NMP region (STAR Methods).

(F) FI profiles measured from the posterior tip of the embryo (*) along the ROI, as shown in (E). Shaded region within arrowheads, NMP region. $n = 10–14$ per marker from 5 to 7 embryos.

due to ongoing morphogenesis. We circumvented this challenge by developing a 2D *in vitro* model of the dorsal neural tube. 2D *in vitro* systems have been used to study signaling and pattern formation in mouse and human gastrulation.[20–22,30,49] In contrast to these systems, our system represents a later developmental stage, early neurulation, and focuses on posterior NMP-derived fates rather than on anterior patterning. Notably, unlike micropatterns, our stencil-based system does not limit growth and cell migration, which was key for obtaining reproducible self-organized patterning. Pattern formation usually occurs concurrently with tissue growth; hence, the system we developed could be widely applicable to other studies of pattern formation, signaling, and growth control.[50]

The stencil-based system allowed us to obtain a quantitative readout of BMP signaling dynamics that we combined with biophysical modeling. Temporal adaptation in the continued presence of ligands, similar to the first phase of BMP signaling that we observed, can arise from diverse cellular mechanisms.[4,51–53] We found that in dorsal neural progenitors, BMP signaling is downregulated by BMP-dependent induction of inhibitors. In contrast to other temporal adaptation mechanisms where the pathway remains refractory over long times, in the dorsal neural tube, the induction of a secondary network operating at slower timescales bypasses such adaptation and initiates a new signaling phase. These connected networks ensure robust sequential relay of signaling in a wide region of parameter space (Figures 4J and 5D).

Our analysis indicates that the two subnetworks are coupled by LMX1A. The second phase is initiated by the dependence of LMX1A induction on a pSMAD1/5 activation threshold in the first phase. The early induction of LMX1A expression that we observed is also supported by single-cell RNA-seq (scRNA-seq) data indicating its expression in early neural plate border cells.[54] Our results further indicate that LMX1A induces positive feedback on its own expression by activating WNT production. Although our results do not rule out the involvement of additional factors in the regulation of LMX1A, we show that our minimal regulatory network, taking into account realistic timescales, is sufficient to explain the observed dynamics. This regulatory logic links BMP and WNT signaling, two pathways that are frequently coupled during development. Our results highlight the strengths of *in vitro* systems for inferring regulatory feedback that can be further studied *in vivo*.

An intrinsic property of the temporal relay mechanism that we uncovered is that it serves as a checkpoint between signaling

events, thereby enforcing a temporal order of downstream patterning events. Cells exiting the NMP state respond to BMP signaling to initiate NC specification.[55] Subsequently, continued NC development and RP-dependent patterning of the dorsal neural progenitor subtypes require a second phase of signaling.[16,42,56] The temporal relay ensures this order and provides a potential mechanism for timing the transition between the neural plate border phase and the subsequent RP-dependent patterning phase.

The relay mechanism allows robust control of distinct features of the signaling dynamics during different phases. The initial phase and concomitant specification of NC are BMP concentration sensitive, in agreement with previous studies that found that the formation of non-neural ectoderm, neural plate border, and neural ectoderm occurs in response to a concentration gradient of BMP.[57–59] In this context, BMP inhibition is thought to be required to achieve the lowest levels of BMP signaling necessary for the acquisition of neural ectoderm identity. By contrast, we show that BMP inhibitors primarily limit the duration of the initial phase and thereby the amount of NC. Our analysis further indicates that during the second phase, the system responds to different BMP concentrations by altering the dynamics of the response. This may explain why both the concentration and duration of BMP signaling affect the acquisition of specific dorsal neural progenitor identities.[9,12]

While the temporal dynamics of morphogen signaling influence development in multiple systems,[1–3] how these dynamics are regulated is often still unclear. A mechanism similar to the one that we describe in the dorsal neural tube may also operate in the ventral neural tube, where SHH signaling is initiated by the notochord and subsequently depends on the specification of a SHH-producing floor plate. BMP4 regulation by positive feedback has also been observed during the exit of ESCs from pluripotency and commitment to differentiation.[60] Thus, temporal relay mechanisms may represent a widespread strategy to time developmental transitions.

Limitations of the study

Our results suggest that multiple BMP inhibitors contribute to pSMAD1/5 dynamics. While we show that *Noggin*, *Smad6*, and *Smad7* are relevant, the effects of other putative inhibitors, alone and in combinations, remain to be tested.

The model captures the minimal set of interactions that yield the observed two-phase dynamics; however, we cannot exclude additional interactions. For instance, additional interactions may account for the slightly faster approach to steady state in the model and improve the correspondence with experimental data. Future work will also be needed to investigate the spatial patterning in this system, its relationship to the temporal dynamics, and its robustness.

We show that BMP signaling is required to initiate the specification of neural plate border during a distinct time window at the end of gastrulation, as previously suggested.[61–63] Our study leaves open the question of how this competence window is regulated (Figure 3A). Previous studies have suggested that this depends on the repression of neural transcription factors that inhibit NC specification, such as PAX6, by fibroblast growth factor (FGF) signaling.[63] Such a mechanism could operate in parallel with the temporal relay in BMP signaling that we describe.

RESOURCE AVAILABILITY

Lead contact

Further information and requests for resources and reagents should be directed to the lead contact, Anna Kicheva (anna.kicheva@ist.ac.at).

Materials availability

Reagents generated in this study can be requested from the lead contact.

Data and code availability

- RNA-seq data has been deposited at GEO and are publicly available as of the date of publication. Accession numbers are listed in the key resources table.
- Code for the quantification of fluorescence intensity (FI) profiles in differentiated cells on stencils, as well as for model simulations, is available on GitHub (https://github.com/dbrueckner/NeuralTubeColonies, https://doi.org/10.5281/zenodo.13335390).
- Any additional information required to reanalyze the data reported in this paper is available from the lead contact upon request.

ACKNOWLEDGMENTS

We thank A. Miller and N. Papalopulu for reagents and J. Briscoe for comments on the manuscript. Work in the A.K. lab is supported by ISTA; the European Research Council under Horizon Europe, grant 101044579; and the Austrian Science Fund (FWF), grant https://doi.org/10.55776/F78. S.L. is supported by Gesellschaft für Forschungsförderung Niederösterreich m.b.H. fellowship SC19-011. D.B.B. was supported by the NOMIS foundation as a NOMIS Fellow and by an EMBO Postdoctoral Fellowship (ALTF 343-2022).

AUTHOR CONTRIBUTIONS

S.L., T.G.M., and M.G.-S. developed methodology and performed experiments; S.L., T.G.M., and D.B.B. analyzed the data; D.B.B. developed the mathematical model; J.M. produced stencils; S.L., T.G.M., D.B.B., A.K., and E.H. interpreted data and designed experiments; and A.K. conceived the study and wrote the manuscript with input from D.B.B., E.H., S.L., and T.G.M. All authors reviewed and edited the manuscript.

DECLARATION OF INTERESTS

The authors declare no competing interests.

STAR★METHODS

Detailed methods are provided in the online version of this paper and include the following:

- KEY RESOURCES TABLE
- EXPERIMENTAL MODEL AND STUDY PARTICIPANT DETAILS
  - ES cell maintenance culture
  - Generation of knockout and transgenic ES cell lines
  - Cell differentiation
  - Mouse strains
- METHOD DETAILS
  - Immunostaining and imaging
  - Time lapse imaging
  - Hybridization chain reaction
  - RT-qPCR
  - RNA-seq sample preparation
  - RNA-seq data analysis
- QUANTIFICATION AND STATISTICAL ANALYSIS
  - Fluorescence intensity profiles in differentiated cells
  - T/BRA and SOX2 colocalization in differentiated cells
  - Fluorescence intensity profiles in embryos
  - Biophysical model of BMP signaling dynamics

SUPPLEMENTAL INFORMATION

Supplemental information can be found online at https://doi.org/10.1016/j.devcel.2024.10.024.

Received: November 13, 2023
Revised: May 8, 2024
Accepted: October 30, 2024
Published: November 26. 2024

REFERENCES

1. Kicheva, A., and Briscoe, J. (2023). Control of tissue development by morphogens. Annu. Rev. Cell Dev. Biol. *39*, 91–121. https://doi.org/10.1146/annurev-cellbio-020823-011522.
2. Economou, A.D., and Hill, C.S. (2020). Temporal dynamics in the formation and interpretation of Nodal and BMP morphogen gradients. Curr. Top. Dev. Biol. *137*, 363–389. https://doi.org/10.1016/bs.ctdb.2019.10.012.
3. Camacho-Aguilar, E., and Warmflash, A. (2020). Insights into Mammalian Morphogen Dynamics from Embryonic Stem Cell Systems, First Edition (Elsevier Inc.). https://doi.org/10.1016/bs.ctdb.2019.11.010.
4. Heemskerk, I., Burt, K., Miller, M., Chhabra, S., Guerra, M.C., Liu, L., and Warmflash, A. (2019). Rapid changes in morphogen concentration control self-organized patterning in human embryonic stem cells. eLife *8*, 1–28. https://doi.org/10.7554/eLife.40526.
5. Teague, S., Primavera, G., Chen, B., Liu, Z.-Y., Yao, L., Freeburne, E., Khan, H., Jo, K., Johnson, C., and Heemskerk, I. (2024). Time-integrated BMP signaling determines fate in a stem cell model for early human development. Nat. Commun. *15*, 1471. https://doi.org/10.1038/s41467-024-45719-9.
6. Wartlick, O., Mumcu, P., Kicheva, A., Bittig, T., Seum, C., Jülicher, F., González-Gaitán, M., Julicher, F., and Gonzalez-Gaitan, M. (2011). Dynamics of Dpp signaling and proliferation control. Science *331*, 1154–1159. https://doi.org/10.1126/science.1200037.
7. Dessaud, E., Yang, L.L., Hill, K., Cox, B., Ulloa, F., Ribeiro, A., Mynett, A., Novitch, B.G., and Briscoe, J. (2007). Interpretation of the sonic hedgehog morphogen gradient by a temporal adaptation mechanism. Nature *450*, 717–720. https://doi.org/10.1038/nature06347.
8. Sagner, A., and Briscoe, J. (2019). Establishing neuronal diversity in the spinal cord: a time and a place. Development *146*, dev182154. https://doi.org/10.1242/dev.182154.
9. Tozer, S., Le Dréau, G., Marti, E., and Briscoe, J. (2013). Temporal control of BMP signalling determines neuronal subtype identity in the dorsal neural tube. Development *140*, 1467–1474. https://doi.org/10.1242/dev.090118.
10. Andrews, M.G., del Castillo, L.M., Ochoa-Bolton, E., Yamauchi, K., Smogorzewski, J., and Butler, S.J. (2017). BMPs direct sensory interneuron identity in the developing spinal cord using signal-specific not morphogenic activities. eLife *6*, 1–24. https://doi.org/10.7554/eLife.30647.
11. Liem, K.F., Tremml, G., and Jessell, T.M. (1997). A role for the roof plate and its resident TGFbeta-related proteins in neuronal patterning in the dorsal spinal cord. Cell *91*, 127–138. https://doi.org/10.1016/s0092-8674(01)80015-5.
12. Duval, N., Vaslin, C., Barata, T.C., Frarma, Y., Contremoulins, V., Baudin, X., Nedelec, S., and Ribes, V.C. (2019). BMP4 patterns Smad activity and generates stereotyped cell fate organization in spinal organoids. Development *146*, dev175430. https://doi.org/10.1242/dev.175430.
13. Kicheva, A., Bollenbach, T., Ribeiro, A., Valle, H.P., Lovell-Badge, R., Episkopou, V., and Briscoe, J. (2014). Coordination of progenitor specification and growth in mouse and chick spinal cord. Science *345*, 1254927. https://doi.org/10.1126/science.1254927.
14. Zagorski, M., Tabata, Y., Brandenberg, N., Lutolf, M.P., Tkačik, G., Bollenbach, T., Briscoe, J., and Kicheva, A. (2017). Decoding of position in the developing neural tube from antiparallel morphogen gradients. Science *356*, 1379–1383. https://doi.org/10.1126/science.aam5887.
15. Liem, K.F., Tremml, G., Roelink, H., and Jessell, T.M. (1995). Dorsal differentiation of neural plate cells induced by BMP-mediated signals from epidermal ectoderm. Cell *82*, 969–979. https://doi.org/10.1016/0092-8674(95)90276-7.
16. Milet, C., and Monsoro-Burq, A.H. (2012). Neural crest induction at the neural plate border in vertebrates. Dev. Biol. *366*, 22–33. https://doi.org/10.1016/j.ydbio.2012.01.013.
17. Kalcheim, C. (2018). Neural crest emigration: from start to stop. Genesis *56*, e23090. https://doi.org/10.1002/dvg.23090.
18. Sauka-Spengler, T., and Bronner-Fraser, M. (2008). A gene regulatory network orchestrates neural crest formation. Nat. Rev. Mol. Cell Biol. *9*, 557–568. https://doi.org/10.1038/nrm2428.
19. Helms, A.W., and Johnson, J.E. (2003). Specification of dorsal spinal cord interneurons. Curr. Opin. Neurobiol. *13*, 42–49. https://doi.org/10.1016/S0959-4388(03)00010-2.
20. Warmflash, A., Sorre, B., Etoc, F., Siggia, E.D., and Brivanlou, A.H. (2014). A method to recapitulate early embryonic spatial patterning in human embryonic stem cells. Nat. Methods *11*, 847–854. https://doi.org/10.1038/nmeth.3016.
21. Morgani, S.M., Metzger, J.J., Nichols, J., Siggia, E.D., and Hadjantonakis, A.K. (2018). Micropattern differentiation of mouse pluripotent stem cells recapitulates embryo regionalized cell fate patterning. eLife *7*, 1–35. https://doi.org/10.7554/eLife.32839.
22. Etoc, F., Metzger, J., Ruzo, A., Ozair, M.Z., Brivanlou, A.H., Siggia, E.D., Etoc, F., Metzger, J., Ruzo, A., Kirst, C., et al. (2016). A balance between secreted inhibitors and edge sensing controls gastruloid self-organization. Dev. Cell *39*, 1–14. https://doi.org/10.1016/j.devcel.2016.09.016.
23. Henrique, D., Abranches, E., Verrier, L., and Storey, K.G. (2015). Neuromesodermal progenitors and the making of the spinal cord. Development *142*, 2864–2875. https://doi.org/10.1242/dev.119768.
24. Nedelec, S., and Martinez-Arias, A. (2021). In vitro models of spinal motor circuit's development in mammals: achievements and challenges. Curr. Opin. Neurobiol. *66*, 240–249. https://doi.org/10.1016/j.conb.2020.12.002.
25. Gouti, M., Tsakiridis, A., Wymeersch, F.J., Huang, Y., Kleinjung, J., Wilson, V., and Briscoe, J. (2014). In vitro generation of neuromesodermal progenitors reveals distinct roles for Wnt signalling in the specification of spinal cord and paraxial mesoderm identity. PLoS Biol. *12*, e1001937. https://doi.org/10.1371/journal.pbio.1001937.
26. Row, R.H., Pegg, A., Kinney, B.A., Farr, G.H., Maves, L., Lowell, S., Wilson, V., and Martin, B.L. (2018). BMP and FGF signaling interact to pattern mesoderm by controlling basic helix-loop-helix transcription factor activity. eLife *7*, 1–27. https://doi.org/10.7554/eLife.31018.
27. Gouti, M., Delile, J., Stamataki, D., Wymeersch, F.J., Huang, Y., Kleinjung, J., Wilson, V., and Briscoe, J. (2017). A gene regulatory network balances neural and mesoderm specification during vertebrate trunk development. Dev. Cell *41*, 243–261.e7. https://doi.org/10.1016/j.devcel.2017.04.002.
28. Gjorevski, N., Nikolaev, M., Brown, T.E., Mitrofanova, O., Brandenberg, N., DelRio, F.W., Yavitt, F.M., Liberali, P., Anseth, K.S., and Lutolf, M.P. (2022). Tissue geometry drives deterministic organoid patterning. Science *375*, eaaw9021. https://doi.org/10.1126/science.aaw9021.
29. Lehr, S., Merrin, J., Kulig, M., Minchington, T., and Kicheva, A. (2024). Protocol for Fabricating Elastomeric Stencils for Patterned Stem Cell Differentiation. STAR Protocols. https://doi.org/10.1016/j.xpro.2024.103187.
30. Britton, G., Heemskerk, I., Hodge, R., Qutub, A.A., and Warmflash, A. (2019). A novel self-organizing embryonic stem cell system reveals signaling logic underlying the patterning of human ectoderm. Development *146*, dev179093. https://doi.org/10.1242/dev.179093.
31. Xue, X., Sun, Y., Resto-Irizarry, A.M., Yuan, Y., Aw Yong, K.M., Zheng, Y., Weng, S., Shao, Y., Chai, Y., Studer, L., et al. (2018). Mechanics-guided embryonic patterning of neuroectoderm tissue from human pluripotent

stem cells. Nat. Mater. *17*, 633–641. https://doi.org/10.1038/s41563-018-0082-9.

32. Paulsen, M., Legewie, S., Eils, R., Karaulanov, E., and Niehrs, C. (2011). Negative feedback in the bone morphogenetic protein 4 (BMP4) synexpression group governs its dynamic signaling range and canalizes development. Proc. Natl. Acad. Sci. USA *108*, 10202–10207. https://doi.org/10.1073/pnas.1100179108.
33. Ybot-Gonzalez, P., Gaston-Massuet, C., Girdler, G., Klingensmith, J., Arkell, R., Greene, N.D.E., and Copp, A.J. (2007). Neural plate morphogenesis during mouse neurulation is regulated by antagonism of Bmp signalling. Development *134*, 3203–3211. https://doi.org/10.1242/dev.008177.
34. Chizhikov, V.V., and Millen, K.J. (2004). Control of roof plate formation by Lmx1a in the developing spinal cord. Development *131*, 2693–2705. https://doi.org/10.1242/dev.01139.
35. Millen, K.J., Millonig, J.H., and Hatten, M.E. (2004). Roof plate and dorsal spinal cord dI1 interneuron development in the Dreher mutant mouse. Dev. Biol. *270*, 382–392. https://doi.org/10.1016/j.ydbio.2004.03.008.
36. Miller, D.S.J., Schmierer, B., and Hill, C.S. (2019). TGF-β family ligands exhibit distinct signalling dynamics that are driven by receptor localisation. J. Cell Sci. *132*, jcs234039. https://doi.org/10.1242/jcs.234039.
37. Parr, B.A., Shea, M.J., Vassileva, G., and McMahon, A.P. (1993). Mouse Wnt genes exhibit discrete domains of expression in the early embryonic CNS and limb buds. Development *119*, 247–261. https://doi.org/10.1242/dev.119.1.247.
38. Zechner, D., Müller, T., Wende, H., Walther, I., Taketo, M.M., Crenshaw, E.B., Treier, M., Birchmeier, W., and Birchmeier, C. (2007). Bmp and Wnt/beta-catenin signals control expression of the transcription factor Olig3 and the specification of spinal cord neurons. Dev. Biol. *303*, 181–190. https://doi.org/10.1016/j.ydbio.2006.10.045.
39. Jho, E.H., Zhang, T., Domon, C., Joo, C.K., Freund, J.N., and Costantini, F. (2002). Wnt / β -Catenin / Tcf signaling induces the transcription of Axin2, a negative regulator of the signaling pathway. Mol. Cell. Biol. *22*, 1172–1183. https://doi.org/10.1128/MCB.22.4.1172-1183.2002.
40. Scott, C.E., Wynn, S.L., Sesay, A., Cruz, C., Cheung, M., Gomez Gaviro, M.-V., Booth, S., Gao, B., Cheah, K.S.E., Lovell-Badge, R., et al. (2010). SOX9 induces and maintains neural stem cells. Nat. Neurosci. *13*, 1181–1189. https://doi.org/10.1038/nn.2646.
41. Cheung, M., Chaboissier, M.-C., Mynett, A., Hirst, E., Schedl, A., and Briscoe, J. (2005). The transcriptional control of trunk neural crest induction, survival, and delamination. Dev. Cell *8*, 179–192. https://doi.org/10.1016/j.devcel.2004.12.010.
42. Lee, K.J., Dietrich, P., and Jessell, T.M. (2000). Genetic ablation reveals that the roof plate is essential for dorsal interneuron specification. Nature *403*, 734–740. https://doi.org/10.1038/35001507.
43. Romanos, M., Allio, G., Roussigné, M., Combres, L., Escalas, N., Soula, C., Médevielle, F., Steventon, B., Trescases, A., and Bénazéraf, B. (2021). Cell-to-cell heterogeneity in sox2 and bra expression guides progenitor motility and destiny. eLife *10*, 1–32. https://doi.org/10.7554/eLife.66588.
44. Roszko, I., Faure, P., and Mathis, L. (2007). Stem cell growth becomes predominant while neural plate progenitor pool decreases during spinal cord elongation. Dev. Biol. *304*, 232–245. https://doi.org/10.1016/j.ydbio.2006.12.050.
45. Lecuit, T., Brook, W.J., Ng, M., Calleja, M., Sun, H., and Cohen, S.M. (1996). Two distinct mechanisms for long-range patterning by decapentaplegic in the Drosophila wing. Nature *381*, 387–393. https://doi.org/10.1038/381387a0.
46. Liu, L., Nemashkalo, A., Rezende, L., Jung, J.Y., Chhabra, S., Guerra, M.C., Heemskerk, I., and Warmflash, A. (2022). Nodal is a short-range morphogen with activity that spreads through a relay mechanism in human gastruloids. Nat. Commun. *13*, 497. https://doi.org/10.1038/s41467-022-28149-3.
47. van Boxtel, A.L., Chesebro, J.E., Heliot, C., Ramel, M.C., Stone, R.K., and Hill, C.S. (2015). A temporal window for signal activation dictates the dimensions of a nodal signaling domain. Dev. Cell *35*, 175–185. https://doi.org/10.1016/j.devcel.2015.09.014.
48. Dickmann, J.E.M., Rink, J.C., and Jülicher, F. (2022). Long-range morphogen gradient formation by cell-to-cell signal propagation. Phys. Biol. *19*. https://doi.org/10.1088/1478-3975/ac86b4.
49. Chhabra, S., Liu, L., Goh, R., Kong, X., and Warmflash, A. (2019). Dissecting the dynamics of signaling events in the BMP, WNT, and NODAL cascade during self-organized fate patterning in human gastruloids. PLoS Biol. *17*, e3000498. https://doi.org/10.1371/journal.pbio.3000498.
50. Minchington, T., Lehr, S., and Kicheva, A. (2023). Control of tissue dimensions in the developing neural tube and somites. Curr. Opin. Syst. Biol. *35*, 100459. https://doi.org/10.1016/j.coisb.2023.100459.
51. Warmflash, A., Zhang, Q., Sorre, B., Vonica, A., Siggia, E.D., and Brivanlou, A.H. (2012). Dynamics of TGF-β signaling reveal adaptive and pulsatile behaviors reflected in the nuclear localization of transcription factor Smad4. Proc. Natl. Acad. Sci. USA *109*, E1947–E1956. https://doi.org/10.1073/pnas.1207607109.
52. Ma, W., Trusina, A., El-Samad, H., Lim, W.A., and Tang, C. (2009). Defining network topologies that can achieve biochemical adaptation. Cell *138*, 760–773. https://doi.org/10.1016/j.cell.2009.06.013.
53. Cohen, M., Kicheva, A., Ribeiro, A., Blassberg, R., Page, K.M., Barnes, C.P., and Briscoe, J. (2015). Ptch1 and Gli regulate Shh signalling dynamics via multiple mechanisms. Nat. Commun. *6*, 6709. https://doi.org/10.1038/ncomms7709.
54. Soldatov, R., Kaucka, M., Kastriti, M.E., Petersen, J., Chontorotzea, T., Englmaier, L., Akkuratova, N., Yang, Y., Häring, M., Dyachuk, V., et al. (2019). Spatiotemporal structure of cell fate decisions in murine neural crest. Science *364*, eaas9536. https://doi.org/10.1126/science.aas9536.
55. Frith, T.J.R., Granata, I., Wind, M., Stout, E., Thompson, O., Neumann, K., Stavish, D., Heath, P.R., Ortmann, D., Hackland, J.O.S., et al. (2018). Human axial progenitors generate trunk neural crest cells in vitro. eLife *7*, 1–27. https://doi.org/10.7554/eLife.35786.
56. Anderson, R.M., Stottmann, R.W., Choi, M., and Klingensmith, J. (2006). Endogenous bone morphogenetic protein antagonists regulate mammalian neural crest generation and survival. Dev. Dyn. *235*, 2507–2520. https://doi.org/10.1002/dvdy.20891.
57. Piacentino, M.L., and Bronner, M.E. (2018). Intracellular attenuation of BMP signaling via CKIP-1/Smurf1 is essential during neural crest induction. PLoS Biol. *16*, e2004425. https://doi.org/10.1371/journal.pbio.2004425.
58. Schumacher, J.A., Hashiguchi, M., Nguyen, V.H., and Mullins, M.C. (2011). An intermediate level of bmp signaling directly specifies cranial neural crest progenitor cells in zebrafish. PLoS One *6*, e27403. https://doi.org/10.1371/journal.pone.0027403.
59. Reichert, S., Randall, R.A., and Hill, C.S. (2013). A BMP regulatory network controls ectodermal cell fate decisions at the neural plate border. Development *140*, 4435–4444. https://doi.org/10.1242/dev.098707.
60. Gunne-Braden, A., Sullivan, A., Gharibi, B., Sheriff, R.S.M., Maity, A., Wang, Y.F., Edwards, A., Jiang, M., Howell, M., Goldstone, R., et al. (2020). GATA3 mediates a fast, irreversible commitment to BMP4-driven differentiation in human embryonic stem cells. Cell Stem Cell *26*, 693–706.e9. https://doi.org/10.1016/j.stem.2020.03.005.
61. Tucker, J.A., Mintzer, K.A., and Mullins, M.C. (2008). The BMP signaling gradient patterns dorsoventral tissues in a temporally progressive manner along the anteroposterior axis. Dev. Cell *14*, 108–119. https://doi.org/10.1016/j.devcel.2007.11.004.
62. Wawersik, S., Evola, C., and Whitman, M. (2005). Conditional BMP inhibition in Xenopus reveals stage-specific roles for BMPs in neural and neural crest induction. Dev. Biol. *277*, 425–442. https://doi.org/10.1016/j.ydbio.2004.10.002.
63. Sasai, N., Kutejova, E., and Briscoe, J. (2014). Integration of signals along orthogonal axes of the vertebrate neural tube controls progenitor

competence and increases cell diversity. PLoS Biol. *12*, e1001907. https://doi.org/10.1371/journal.pbio.1001907.

64. Magin, T.M., McWhir, J., and Melton, D.W. (1992). A new mouse embryonic stem cell line with good germ line contribution and gene targeting frequency. Nucleic Acids Res. *20*, 3795–3796. https://doi.org/10.1093/nar/20.14.3795.
65. Concordet, J.P., and Haeussler, M. (2018). CRISPOR: intuitive guide selection for CRISPR/Cas9 genome editing experiments and screens. Nucleic Acids Res. *46*, W242–W245. https://doi.org/10.1093/nar/gky354.
66. Ran, F.A., Hsu, P.D., Wright, J., Agarwala, V., Scott, D.A., and Zhang, F. (2013). Genome engineering using the CRISPR-Cas9 system. Nat. Protoc. *8*, 2281–2308. https://doi.org/10.1038/nprot.2013.143.
67. Miller, A., Biga, V., Rowntree, A., Chhatriwala, M., Woods, F., Marinopoulou, E., Kamath, A., Vallier, L., and Papalopulu, N. (2023). NGN3 oscillatory expression controls the timing of human pancreatic endocrine differentiation. Preprint at bioRxiv. https://doi.org/10.2139/ssrn.4658844.
68. Folch, A., Jo, B.-H., Hurtado, O., Beebe, D.J., and Toner, M. (2000). Microfabricated elastomeric stencils for micropatterning cell cultures. J. Biomed. Mater. Res. *52*, 346–353. https://doi.org/10.1002/1097-4636(200011)52:2<346::AID-JBM14>3.0.CO;2-H.
69. Lewis, A.E., Vasudevan, H.N., O'Neill, A.K., Soriano, P., and Bush, J.O. (2013). The widely used Wnt1-Cre transgene causes developmental phenotypes by ectopic activation of Wnt signaling. Dev. Biol. *379*, 229–234. https://doi.org/10.1016/j.ydbio.2013.04.026.
70. Arnold, K., Sarkar, A., Yram, M.A., Polo, J.M., SenGupta, S., Seandel, M., Geijsen, N., and Hochedlinger, K. (2011). Sox2+ adult stem/progenitor cells are important for tissue regeneration and survival of mice. Cell Stem Cell *9*, 317–329. https://doi.org/10.1016/j.stem.2011.09.001.Sox2.
71. Stafford, D.A., Brunet, L.J., Khokha, M.K., Economides, A.N., and Harland, R.M. (2011). Cooperative activity of noggin and gremlin 1 in axial skeleton development. Development *138*, 1005–1014. https://doi.org/10.1242/dev.051938.
72. Pierani, A., Moran-Rivard, L., Sunshine, M.J., Littman, D.R., Goulding, M., and Jessell, T.M. (2001). Control of interneuron fate in the developing spinal cord by the progenitor homeodomain protein Dbx1. Neuron *29*, 367–384.
73. Balaskas, N., Ribeiro, A., Panovska, J., Dessaud, E., Sasai, N., Page, K.M., Briscoe, J., and Ribes, V. (2012). Gene regulatory logic for reading the Sonic Hedgehog signaling gradient in the vertebrate neural tube. Cell *148*, 273–284. https://doi.org/10.1016/j.cell.2011.10.047.
74. Choi, H.M.T., Schwarzkopf, M., Fornace, M.E., Acharya, A., Artavanis, G., Stegmaier, J., Cunha, A., and Pierce, N.A. (2018). Third-generation in situ hybridization chain reaction: multiplexed, quantitative, sensitive, versatile, robust. Development *145*, 1–10. https://doi.org/10.1242/dev.165753.
75. Love, M.I., Huber, W., and Anders, S. (2014). Moderated estimation of fold change and dispersion for RNA-seq data with DESeq2. Genome Biol. *15*, 550. https://doi.org/10.1186/s13059-014-0550-8.
76. Robinson, M.D., McCarthy, D.J., and Smyth, G.K. (2010). edgeR: A Bioconductor package for differential expression analysis of digital gene expression data. Bioinformatics *26*, 139–140. https://doi.org/10.1093/bioinformatics/btp616.
77. Schindelin, J., Arganda-Carreras, I., Frise, E., Kaynig, V., Longair, M., Pietzsch, T., Preibisch, S., Rueden, C., Saalfeld, S., Schmid, B., et al. (2012). Fiji: an open-source platform for biological-image analysis. Nat. Methods *9*, 676–682. https://doi.org/10.1038/nmeth.2019.
78. Wymeersch, F.J., Huang, Y., Blin, G., Cambray, N., Wilkie, R., Wong, F.C.K., and Wilson, V. (2016). Position-dependent plasticity of distinct progenitor types in the primitive streak. eLife *5*, e10042. https://doi.org/10.7554/eLife.10042.
79. Antebi, Y.E., Linton, J.M., Klumpe, H., Bintu, B., Gong, M., Su, C., McCardell, R., and Elowitz, M.B. (2017). Combinatorial signal perception in the BMP pathway. Cell *170*, 1184–1196.e24. https://doi.org/10.1016/j.cell.2017.08.015.
80. Kicheva, A., Pantazis, P., Bollenbach, T., Kalaidzidis, Y., Bittig, T., Jülicher, F., and González-Gaitán, M. (2007). Kinetics of morphogen gradient formation. Science *315*, 521–525. https://doi.org/10.1126/science.1135774.
81. Müller, P., Rogers, K.W., Jordan, B.M.B., Lee, J.S., Robson, D., Ramanathan, S., and Schier, A.F. (2012). Differential diffusivity of Nodal and lefty underlies a reaction-diffusion patterning system. Science *336*, 721–724. https://doi.org/10.1126/science.1221920.
82. Pomreinke, A.P., Soh, G.H., Rogers, K.W., Bergmann, J.K., Bläßle, A.J., and Müller, P. (2017). Dynamics of BMP signaling and distribution during zebrafish dorsal-ventral patterning. eLife *6*, 1–30. https://doi.org/10.7554/eLife.25861.
83. Harris, C.R., Millman, K.J., van der Walt, S.J., Gommers, R., Virtanen, P., Cournapeau, D., Wieser, E., Taylor, J., Berg, S., Smith, N.J., et al. (2020). Array programming with NumPy. Nature *585*, 357–362. https://doi.org/10.1038/s41586-020-2649-2.
84. Press, W.H., Teukolsky, S.A., Vetterling, W.T., and Flannery, B.P. (2002). Numerical Recipes: the Art of Scientific Computing, Second Edition (Cambridge University Press).
85. Werner, S. (2016). Growth and Scaling during Development and Regeneration. Preprint at arXiv. https://doi.org/10.48550/arXiv.1608.06918.

STAR★METHODS

KEY RESOURCES TABLE

REAGENT or RESOURCE	SOURCE	IDENTIFIER
Antibodies		
Mouse AP-2ALPHA	Santa Cruz Biotechnology	Cat# SC-12726; RRID: AB_667767
Rabbit ATOH1	Proteintech	Cat# 21215-1-AP; RRID: AB_10733126
Rabbit LMX1A	Atlas Antibodies	Cat# HPA030088; RRID: AB_10601106
Mouse MASH1 (ASCL1)	BD Biosciences	Cat# 556604; RRID: AB_396479
Mouse OLIG3	Abcam	Cat# ab168573; RRID: AB_2620178
Rabbit Phospho-SMAD1/5	Cell Signaling Technology	Cat# 9516; RRID: AB_491015
Goat SOX2	R&D Systems	Cat# AF2018; RRID: AB_355110
Mouse SOX2	R&D Systems	Cat# MAB2018; RRID: AB_358009
Rabbit SOX9	Cell Signaling Technology	Cat# 82630; RRID: AB_2665492
Mouse SOX10	Santa Cruz Biotechnology	Cat# sc-365692; RRID: AB_10844002
Rabbit WNT1	Abcam	Cat# ab15251; RRID: AB_301792
Sheep ERBB3/HER3	R&D Systems	Cat# AF4518; RRID: AB_2099728
Sheep GFP	Bio-Rad	Cat# 4745-1051; RRID: AB_619712
Goat T/BRACHURY	R&D Systems	Cat# AF2085; RRID: AB_2200235
Rabbit DBX1	Pierani et al.[72]	N/A
Goat OLIG2	R&D Systems	Cat# AF2418; RRID: AB_2157554
Mouse NKX6.1	DSHB	Cat# F55A10; RRID: AB_532378
Chemicals, peptides and recombinant proteins		
0.1% Gelatin in H_2O	Stemcell Technologies	07903
2-Mercaptoethanol (50 mM)	Gibco	31350010
Accutase	Gibco	A1110501
B-27 Supplement (50x), serum free	Gibco	17504001
bFGF	R&D Systems	3139–FB–025
BMP4	R&D Systems	5020-BP-010
WNT3A	R&D Systems	1324-WNP-010
BSA	Sigma-Aldrich	A3156
CHIR99021	Axon	1386
DMEM/F-12	Gibco	21331020
FBS for ESC (30 min. 56°C heat inactivated)	Pan Biotech	P30-2602
Gelatin Solution, 2% in H_2O	Sigma-Aldrich	G1393
GlutaMAX	Gibco	35050061
L-Glutamine	Gibco	25030024
LDN-193189	Tocris	6053
LIF	Sigma-Aldrich	ESG1107
MEM Non-Essential Amino Acids Solution	Gibco	11140035
N-2 Supplement (100x)	Gibco	17502001
Neurobasal Medium	Gibco	21103049
PD98059	Cell Signaling Technology	9900
Penicillin-Streptomycin	Gibco	15140122
Retinoic Acid (RA)	Sigma-Aldrich	R2625
ROCK inhibitor	Tocris	1254
Doxycycline hyclate	Sigma-Aldrich	D9891
Cycloheximide	Cell Signaling Technology	2112S

(*Continued on next page*)

Continued

REAGENT or RESOURCE	SOURCE	IDENTIFIER
Puromycin	Gibco	A11138-03
KnockOut DMEM	Gibco	10829018
Laminin	Sigma-Aldrich	L2020
ProLong Gold Antifade Mountant	Invitrogen	P36930
Ibidi Mounting Medium	Ibidi	50001
Sucrose	Sigma-Aldrich	S9378
Paraformaldehyde	Sigma-Aldrich	P6148
O.C.T. compound	Tissue-Tek	R1180
Proteinase K Solution, RNA grade	Invitrogen	25530049
Tamoxifen	Sigma-Aldrich	T5648
Critical commercial assays		
PureLink RNA Mini Kit	Invitrogen	12183025
PureLink DNase Set	Invitrogen	12185010
SuperScript III First-Strand Synthesis	Invitrogen	18080051
Phusion High-Fidelity DNA Polymerase	New England Biolabs	M0530
Q5 High-Fidelity DNA Polymerase	New England Biolabs	M0491
T4 DNA Ligase	Takara	2011A
In-Fusion HD Cloning Kit	Takara	639650
LightCycler 480 SYBR Green I Master	Roche Life Science	04707516001
HCR™ RNA-FISH Bundle	Choi et al.[74]	N/A
Deposited data		
RNA sequencing data	https://www.ncbi.nlm.nih.gov/geo	GEO: GSE247069
Experimental models: Cell lines		
Mouse: HM1 ESCs	Magin et al.[64]	N/A
Mouse: *Lmx1a* KO HM1 ESCs	This paper	N/A
Mouse: *Noggin* KO HM1 ESCs	This paper	N/A
Mouse: *Smad6/7* DKO HM1 ESCs	This paper	N/A
Mouse: *Sox9* KO HM1 ESCs	This paper	N/A
Mouse: TetON-Lmx1a-IRES-GFP HM1 ESCs	This paper	N/A
Mouse: mScarlet-I-NLS HM1 ESCs	This paper	N/A
Experimental models: Organisms/strains		
Mouse: B6.Cg-E2f1$^{Tg(Wnt1-cre)2Sor}$/J	The Jackson Laboratory	RRID:IMSR_JAX:022501
Mouse: B6;129S-Sox2$^{tm1(cre/ERT2)Hoch}$/J	The Jackson Laboratory	RRID:IMSR_JAX:017593
Mouse: *Nog*$^{tm1.1Rmh}$/J	The Jackson Laboratory	RRID:IMSR_JAX:016117
Oligonucleotides		
Noggin gRNA targeting sequence: GCTCGGGGGCCACTACGACCCGG	This paper	N/A
Smad6 gRNA targeting sequence 1: CAAACCTAGCTGGGACCGCGGGG	This paper	N/A
Smad6 gRNA targeting sequence 2: GAGTCCCGAGGCGGCGTACCGGG	This paper	N/A
Smad7 gRNA targeting sequence 1: CCAAACGATCTGCGCTCGTCCGG	This paper	N/A
Smad7 gRNA targeting sequence 2: CTAGTTCACAGAGTCGACTAAGG	This paper	N/A
Lmx1a gRNA targeting sequence 1: GTTGGACGGCCTGAAGATGGAGG	This paper	N/A
Lmx1a gRNA targeting sequence 2: CTTCTTGTCCCGGTAGAAGCAGG	This paper	N/A

(*Continued on next page*)

Continued

REAGENT or RESOURCE	SOURCE	IDENTIFIER
Sox9 gRNA targeting sequence 1: GCTGGTACTTGTAATCGGGGTGG	This paper	N/A
Sox9 gRNA targeting sequence 2: GTCGTATTGCGAGCGGGTGATGG	This paper	N/A
Recombinant DNA		
Plasmid: pSpCas9(BB)-2A-Puro (PX459) v2.0	Addgene	#62988
Plasmid: pSpCas9(BB)-2A-GFP (PX458)	Addgene	#48138
Plasmid: PB-TRE-Lmx1a-IRES-GFP-EF1a-rtTA	This paper	N/A
Plasmid: PB-TRE-EGFP-EF1a-rtTA	Addgene	#104454
Plasmid: CAG-NLS-mScarlet-I-NLS-IRES-Puromycin	Miller et al.[67]	N/A
Software and algorithms		
CRISPOR tool	Concordet and Haeussler[65]	N/A
Trim galore V0.5.0	https://github.com/FelixKrueger/TrimGalore	N/A
STAR aligner v2.6.0c	https://github.com/alexdobin/STAR	N/A
R (v4.3.0)	https://www.r-project.org	N/A
DESeq2	Love et al.[75]	N/A
edgeR	Robinson et al.[76]	N/A
Fiji	Schindelin et al.[77]	N/A
Python 3	https://www.python.org	N/A
Imaris	https://imaris.oxinst.com	N/A
Other		
CellBIND surface, 60 mm	Corning	3295
CellBIND surface, 100 mm	Corning	3296
CellBIND surface, 12-well	Corning	3336
μ-slide 2-well, ibiTreat	ibidi	80286
CYTOOchips Arena A	Cytoo	10-020-00-18
TC10 counting slides	Bio-Rad	1450011
Mouse ESC Nucleofector® Kit	Lonza	LONVPH-1001

EXPERIMENTAL MODEL AND STUDY PARTICIPANT DETAILS

ES cell maintenance culture

Mouse HM1 ES cell[64] background was used for all experiments. All cell culture reagents and plastics are listed in the key resources table. ES cells were maintained on CellBIND dishes (Corning) coated with 0.1% gelatin (Sigma) at 37°C 5% CO_2.

Stem cells were maintained in N2B27 + 2i + LIF media. N2B27 is composed of 1:1 mix of DMEM/F-12 (Gibco) and Neurobasal medium (Gibco), 1x N2 (Gibco), 1x B27 (Gibco), 0.08 % BSA (Sigma), 2 mM L-Glutamine or Glutamax (Gibco), 100 U/ml Penicillin-Streptomycin (Gibco), 0.1 mM 2-Mercaptoethanol (Gibco). For 2i + LIF, N2B27 was supplemented with 3μM CHIR99021 (Axon), 1μM PD98059 (Cell Signaling Technology) and 1,000 U/ml LIF (Chemicon). Media was exchanged daily.

Cells were passaged every 2-3 days by incubation with Accutase (Gibco) for 2-3 min at 37°C, dissociated to a single cell suspension. Cells were counted using a cell counter (BioRad), collected by centrifugation at 1000rpm for 4 min, then seeded at a density of 120-200x10^3 cells per 6 cm plate. Cell lines were routinely tested and confirmed negative for mycoplasma.

Generation of knockout and transgenic ES cell lines

To generate knockout cell lines, gRNAs were designed using the CRISPOR tool[65] against sequences in exons 1 to 3 (key resources table). One to two gRNAs per gene with MIT score >70 were chosen, phosphorylated oligos ordered from Sigma and cloned into pSpCas9(BB)-2A-Puro (PX459) V2.0 (Addgene, Plasmid #62988) or pSpCas9(BB)-2A-GFP (PX458) (Addgene, Plasmid #48138) according to standard protocol.[66]

To generate the TetON-Lmx1a-IRES-GFP cell line, the mouse *Lmx1a* CDS was amplified from cDNA and IRES-GFP was amplified from a commonly used plasmid in the lab. PB-TRE-EGFP-EF1a-rtTA (Addgene, Plasmid #104454) was digested with NheI and KpnI and the *Lmx1a* CDS and IRES-GFP fragments were inserted using the In-Fusion HD Cloning kit (Takara).

The CAG-NLS-mScarlet-I-NLS-IRES-Puromycin plasmid used for generating a reporter cell line (referred to as mScarlet-I-NLS in this study) was previously described[67] and obtained as a gift from A. Miller and N. Papalopulu.

A total of 3-4 μg of plasmid DNA was electroporated into 3-4x10^6 early passage ES cells using the Amaxa Nucleofector II (Lonza) program A-023. Electroporated cells were seeded onto a gelatin coated 10cm CellBind plate (Corning) and cultured in 2i+LIF. The following day, 2i+LIF was supplemented with 1-2 μg/mL puromycin (Sigma) for 48 hours (or longer for the TetON-Lmx1a-IRES-GFP and mScarlet-I-NLS lines), or FACS sorted for GFP expression. For the knockout and TetON-Lmx1a-IRES-GFP line, after additional 5-7 days in 2i + LIF, individual colonies were picked into 96-well plates, dissociated using Accutase and plated onto feeder cells (mouse embryonic fibroblasts (MEFs) isolated from E13.5 mouse embryos mitotically inactivated by Mitomycin C treatment) in 96-well plates in ESC medium + 1,000 U/ml LIF. ESC medium comprises KnockOut-DMEM, 1% FBS (Pan Biotech), 100 U/ml Penicillin-Streptomycin (Gibco), 2 mM L-Glutamine or Glutamax), 1x MEM Non-Essential Amino Acids Solution (Gibco) and 0.2 mM 2-Mercaptoethanol (Gibco). *Lmx1a*-overexpressing clones were grown in puromycin until the start of an experiment. *Lmx1a* expression was induced using 2μg/ml doxycycline at t = 0h. The population of mScarlet-I-NLS cells was grown in puromycin until the start of the differentiation experiment.

A replica plate without feeder cells was used for DNA isolation and genotyping. Knockouts were identified as lines that had large deletions and resulting frameshift mutations in early exons. Absence of gene product was confirmed by immunofluorescence where antibodies were available. Selected clones were expanded on feeder cells in ESC medium for 2-3 passages and then transferred to N2B27 + 2i + LIF.

Cell differentiation

For differentiation experiments, ~2,600 cells per cm^2 were plated in N2B27 medium + LIF (1,000 U/ml) on CellBIND dishes pre-coated with 0.1 % gelatin (Sigma) and incubated overnight. Differentiation was initiated by adding N2B27 medium supplemented with 10 ng/ml bFGF for 48 hours, followed by a pulse of 10 ng/ml bFGF + 5 μM CHIR99021 for 24 h.[25] Subsequently, the medium was changed to N2B27 supplemented with 100 nM RA and BMP4 at the indicated concentration for the indicated amount of time. Addition of RA + BMP4 is considered as t=0h.

To differentiate cells on stencils, PDMS stencils were fabricated to fit 2-well μ-slide ibiTreat dishes following a custom protocol[29] based on Folch et al.[68] Stencils wells were 300 μm in diameter, 210 μm in height, and were spaced 600 μm apart. Prior to plating cells on stencils, 1.5–1.8 million cells were plated on 100 mm CellBIND dishes and cultured overnight in N2B27 medium + LIF (1,000 U/ml), and then in N2B27 medium + 10 ng/ml bFGF for 24h. Cells were then replated on stencils on the second day of bFGF treatment. For this, stencils were placed into the wells of 2-well μ-slide ibiTreat dishes pre-coated with 0.1 % gelatin (Millipore) and dried for ~30 min. Stencils were covered with a 1:1 mix of Neurobasal Media (Gibco) and DMEM/F12 (Gibco) medium and dishes were placed into a desiccator to remove air bubbles. After 24 h in N2B27 + bFGF, cells were dissociated from the 100 mm dishes and 2.8–3 M cells per well were seeded on the prepared 2-well dishes in N2B27 medium with 10 ng/ml bFGF + 10 μM Y-27632 ROCK inhibitor (Tocris) media for 3 h. Cells were then washed and further cultured in N2B27 + 10 ng/ml bFGF. The next day, the stencils were removed, and the differentiation protocol continued with the media change as described above from day 3 onwards.

To differentiate cells on restricted micropatterned surfaces (Figure S1D), we used micropatterned glass chips Arena A 500 μm diameter (Cytoo). Chips were coated overnight with 1:40 dilution of laminin (Sigma) in PBS in a humid chamber, then placed into the well of a 6-well dish and washed 2x with PBS. Similar to plating on stencils, 3 M cells on the second day of bFGF treatment were plated onto the chips in N2B27 medium with 10 ng/ml bFGF + 10 μM Y-27632 ROCK inhibitor (Tocris) and washed 3 h after plating.

To inhibit BMP signaling, cell culture medium was supplemented with 1 or 3 μM LDN-193189 (Tocris) at the indicated times. In Figure S3, colonies were treated with 10 μM Y-27632 ROCK inhibitor (Tocris).

To measure the LMX1A half-life, cells were treated at t = 72h with 10 μM cycloheximide (Cell Signaling Technology).

Mouse strains

All work with animals was approved under the license BMWFW-66.018/0006-WF/V/3b/2016 from the Austrian Bundesministerium für Wissenschaft, Forschung und Wirtschaft. All procedures were performed in accordance with the relevant regulations. The CD-1 outbred mouse strain (Charles River) was used to obtain wildtype embryos for analysis. Transgenic strains were maintained onto CD-1 background. The following strains and respective genotyping protocols were previously described: Wnt1-Cre2 (JAX: 022501, Lewis et al.[69]), Sox2CreERT2 (JAX: 017593, Arnold et al.[70]), *Nog*^{Flox} (JAX: 016117, Stafford et al.[71]). Experimental animals were kept in an individually ventilated caging (IVC) system with a 12h light/12h dark cycle and temperature ranging from 21–25°C. 4–5 mice were housed per 501 cm^2 cage (GM500), and with free access to water and food. For timed matings, 2–3 females > 10 weeks old were housed together with 1 male and checked for vaginal plugs twice daily. Plug-positive females were separated into individual cages and supplied with enriched environment. Pregnant mothers were intraperitoneally injected with 4mg tamoxifen in sunflower oil at the indicated developmental stages and the cages were kept in ventilated cabinets until the day of sacrificing. Embryos were dissected and fixed according to developmental stage, and embedded in gelatin for cryosectioning. Yolk sacs were collected for genotyping.

METHOD DETAILS

Immunostaining and imaging

Cultured cells were fixed for 18 min on ice with cold 4% PFA. Samples were incubated in PBST (PBS + 0.1% Triton X-100) 3x 5-10 min, then 2-3 h in blocking buffer (PBST + 1% BSA) at room temperature, followed by incubation with primary antibodies overnight at 4°C, 3 washes 5-10 min each in PBST, secondary antibodies and DAPI (Sigma) for 2 h at room temperature, 3 washes 5-10 min each in PBST. Samples were stored in Ibidi mounting medium (Ibidi). Antibodies used are listed in the key resources table. The DBX1 antibody was a gift from A. Pierani.[72]

Mouse embryos were fixed and cryoprotected as previously described.[73] For immunostaining of transverse sections, slides were incubated for 20 min at 42°C in PBS, then in PBS + 0.1 % Tween + 1 % BSA for 2 h at room temperature, in primary antibody solution overnight at 4°C, washed 3x for 5-10 min with PBS + 0.1 % Tween, in secondary antibodies and DAPI for 2 h at room temperature, then washed 3x for 5-10 min with PBST and mounted in ProLong Antifade Mounting medium (Invitrogen).

For whole mount embryo preparations, E8.5 embryos were fixed for 50 min in 4 % PFA then washed 3x 5-10 min in PBS + 0.1 % Tween, and dehydrated using a Methanol series (25, 50, 75, 100 %) and stored at -20°C. For immunostaining, embryos were rehydrated, washed in PBST and incubated in primary antibody at 4°C overnight, followed by 3x 5 min washes in PBST and a long wash overnight, followed by overnight incubation in secondary antibody solution, 3x 5-10 min washes and another overnight wash. Embryos were mounted in Prolong Antifade Mounting Medium.

Images of ESC colonies were acquired on an inverted Zeiss LSM800 confocal microscope with GaAsP PMTs, using Plan Apo 10x/NA 0.45 or Plan Apo 20x/NA 0.8 objectives, z-stacks with at least 15% overlap. Whole mount (Figure 7) and *Lmx1a* (Figure S1) HCRs were imaged on a Nikon Spinning Disk CSU-W1 with a pinhole size of 25 μm using CFI Apo LWD λ S 20x WI/NA 0.95 water and CFI Plan Apo λ 60x oil/NA 1.4 oil objectives. Tile scans were stitched using Imaris stitcher.

Time lapse imaging

For the live imaging, wildtype HM1 and mScarlet-I cell lines were differentiated as above until they were replated on stencils, where wildtype and mScarlet-I-NLS cells in suspension were combined at a 7:3 ratio. The differentiation was then continued and at t=0h cells in one well of the IBIDI 2-well slide were supplemented with 0.5 ng/ml BMP4 + RA and in the other with 3 ng/ml BMP4 + RA. Colonies were imaged from t=8h to 24 h with images taken every 20 min on a Nikon CSU-W1 spinning disc confocal microscope with incubation chamber at 37°C and 5% CO_2 which was allowed to equilibrate for 1h prior to imaging. Imaging was conducted using a CFI Plan Apo λ 20x air / 0.95/ 0.17-0.25vmm (MRD00205) with a pinhole diameter of 50 μm. Following live imaging, colonies were fixed, immunostained and reimaged using the saved positions from the time lapse data. AP2ALPHA positive neural crest progenitors were identified and tracked back to their starting positions.

Hybridization chain reaction

HCR probes (HCR v3.0[74]) were ordered from Molecular Instruments. For HCR on 2-well ibidi slides, the "Protocol for mammalian cell on a chambered slide" (https://www.molecularinstruments.com/hcr-rnafish-protocols, Revision Number: 4) was followed with minor modifications. Briefly, cells were washed with PBS, fixed with 4% PFA for 20 min on ice, washed 3x with PBS, and stored in 70 % EtOH at -20°C overnight to a maximum of 3 weeks. EtOH was aspirated and samples were dried for ~30 min at room temperature. After 2 washes with 2x SSC, samples were prehybridized in probe hybridization buffer at 37°C for 30-60 min. Samples were incubated with 1.2 pmol of each probe at 37°C overnight. Following 4x 5 min washes with probe wash buffer at 37°C and 2x 5 min washes with 5x SSCT at room temperature, samples were pre-amplified in amplification buffer for 30-60 min at room temperature. Samples were incubated overnight with 18 pmol of each snap-cooled hairpin in amplification buffer at room temperature. After 2x 5 min washes with 5x SSCT at room temperature, samples were incubated for 5 min in 5x SSCT with DAPI, followed by another 2x 5min washes with 5x SSCT. Ibidi mounting medium was added to the samples that were then stored at 4°C prior to imaging. For performing immunofluorescence staining post HCR, after the washes cells were washed 3x 5 min with PBST and then subjected to the immunostaining protocol described above, starting from incubation in blocking buffer.

For HCR on tissue sections, "In situ HCR v3.0 protocol for sample on slide" (https://www.molecularinstruments.com/hcr-rnafish-protocols, Revision Number: 4) was followed with minor modifications. Briefly, embryos were dissected in cold PBS and fixed for 50 min in 4 % cold PFA on ice. Embryos were washed 3x 5 min in cold PBS and incubated in 15 % sucrose at 4°C for 1-6 h. Brachial regions were further incubated in 30 % sucrose (except for e8.5 where whole embryos were incubated) for 2 h - overnight. The tissue was then incubated in a 1:1 mix of 30 % sucrose:OCT for 1-2 h, then in OCT for 1-2 h, then transferred to a mold, and frozen on dry ice. OCT blocks were cryosectioned into 14 μm thick sections and stored at -80°C. For HCR, slides were air-dried for 5-10 min and post-fixed for 15 min in 4 % PFA. Slides were washed 2x 10 min in cold PBS and then incubated in 70 % EtOH for 10 min on ice, followed by incubation in 70 % EtOH for 4 h - overnight at -20°C. Slides were washed 3x in Hybridization Wash Buffer (10 % Formamide in 2x SSC), dried and then incubated in probe hybridization buffer for 10 min at 37°C in a humidified chamber. The tissue was incubated overnight in hybridization buffer containing 0.4 pmol of each probe mixture, which was covered with Parafilm to prevent evaporation. Slides were washed in probe wash buffer for 5min, then increasing % of 5x SSCT in probe wash buffer 15 min each until 100% 5x SSCT 15 min, all at 37°C, and 5x SSCT for 5 min at room temperature. Slides were dried and incubated in amplification buffer for

30 min at RT, followed by incubation with 6 pmol of each hairpin overnight, covered with Parafilm to prevent evaporation. Following 1x 5 min wash with 5x SSCT + DAPI, 2x 30 min 5x SSCT, 1x 5 min SSCT, all at RT, the tissue on the slide was covered with Prolong Gold and a glass coverslip.

For HCR of whole-mount mouse embryos, "HCR RNA-FISH protocol for whole-mount mouse embryos" (https://www.molecularinstruments.com/hcr-rnafish-protocols, Revision Number: 9) was followed with minor modifications. Briefly, e8.5 mouse embryos were dissected in cold 4 % PFA and fixed overnight at 4°C. Embryos were washed 2x 5 min with PBST, dehydrated with a series of graded methanol/PBST washes on ice 10 min each, then stored in 100 % methanol at -20°C. After rehydration to PBST with a series of graded methanol/PBST washes on ice 10 min each, embryos were washed 2x 5 min in PBST at room temperature and then incubated in 10 μg/ml proteinase K in PBST for 10 min at room temperature. Embryos were washed 2x 5 min with PBST, postfixed with 4 % PFA for 20 min at room temperature, and again washed 3x 5 min with PBST. Embryos were incubated first for 5 min, then for 30 min in probe hybridization buffer at 37°C, and then incubated overnight in probe hybridization buffer containing 2 pmol of each probe set. This was followed by 4x 15 min washes with probe wash buffer at 37°C, 2x 5 min washes with 5x SSCT at room temperature, 1x 5-30 min in amplification buffer at room temperature, incubation overnight in amplification buffer containing 30 pmol of each hairpin. On the next day, embryos were washed 2x 5 min in 5x SSCT, 1x 30 min in 5x SSCT + DAPI, 1x 30 min in 5x SSCT, 1x 5 min in 5x SSCT and then mounted on a glass slide.

RT-qPCR

RNA was extracted from cells cultured in 12-well plates using the Purelink RNA Mini Kit (Invitrogen). DNA was removed by incubating the preparation on the column with Purelink DNase (Invitrogen). RNA was quantified and stored at -80C. cDNA was generated from 500 - 2000 ng total RNA using SuperScript III (Invitrogen) with random hexamer primers. Quantitative RT-PCR was performed in triplicates using Roche Lightcycler 480 SYBR Green in 384-well format.

RNA-seq sample preparation

Cells differentiated on stencils were dissociated into single cells and pelleted by centrifugation. Three biological replicates per timepoint and condition were collected. Sequencing libraries were prepared by the VBC Sequencing facility using NEB poly-A stranded kit. Pooled libraries were sequenced on the NextSeq2000 P3 (paired-end 50bp reads).

RNA-seq data analysis

RNA-seq reads were trimmed using Trim galore v0.5.0 (https://github.com/FelixKrueger/TrimGalore), aligned to the GRCm38 genome using STAR aligner v2.6.0c (https://github.com/alexdobin/STAR) and counted using GeneCounts. Gene count tables were imported into R (v4.3.0) (R Core Team) and converted to a DESeq data set using DESeqDataSetFromMatrix (https://bioconductor.org/packages/release/bioc/html/DESeq2.html). Log_2 fold change relative to BMP4 concentration 0 ng/ml or time =0h (as indicated) was calculated using DESeq2[75] library in R. Regularized log transform of counts was used for heatmaps when comparing over time. Heatmaps were generated using the pheatmap library in R. FPKM values were generated using the edgeR library in R.[76]

RNA-sequencing data generated in this study is available at GEO (Gene Expression Omnibus, https://www.ncbi.nlm.nih.gov/geo/), accession number GSE247069.

QUANTIFICATION AND STATISTICAL ANALYSIS

Fluorescence intensity profiles in differentiated cells

Fluorescence intensity (FI) profiles in maximum intensity projection images of antibody stainings of colonies differentiated on stencils were measured as a function of the radial distance from the colony center using a custom script in Python 3 (https://github.com/dbrueckner/NeuralTubeColonies, https://doi.org/10.5281/zenodo.13335390). Specifically, we identify the position of the colony center $\boldsymbol{X}_c$ using the SOX2 FI by taking the mean position $\boldsymbol{X_i} = (x, y)$ of all pixels multiplied by their respective SOX2 FI $FI_{\mathrm{SOX2}}(\boldsymbol{X}_i)$: i.e.

$$\boldsymbol{X}_c = \sum_{i=0}^{N^2} \boldsymbol{X}_i FI_{\mathrm{SOX2}}(\boldsymbol{X}_i)$$

for an image with N x N pixels with indices i. Thus, the radial distance of every pixel from the inferred colony center is $r_i = \sqrt{(\boldsymbol{X}_i - \boldsymbol{X}_c)^2}$. The radial fluorescence intensity profile of the protein or gene of interest is then measured using the average FI as a function of the radial coordinate $f_\alpha(r) = \langle FI_\alpha(\boldsymbol{X}) | r = r_i \rangle$. Colonies that were strongly asymmetric due to distortions during the culture or sample preparation process were excluded from analysis.

After the spatial FI profiles were measured, the maximum intensity value of each profile was identified and used as a data point in further analysis. Within a given experiment that includes different conditions or time points, all colonies were processed and imaged in an identical manner and therefore the fluorescence intensities are comparable. Within each experiment, background FI was determined from a time point or condition where there was no expression of the analyzed marker, and subtracted from data. To combine data from independent experiment repeats, data points were normalized to the experiment mean for a defined time point (in most cases we used the time point of maximal FI across the time course) or condition (in most cases, we used 0.5ng/ml BMP4).

To obtain an estimate of the number of cells expressing a given protein of interest, we measured the area occupied by cells positively stained for that protein in maximum projection images. Threshold fluorescence intensities were determined using a negative control sample with a custom script in Python 3 using Matplotlib's imshow() and applied to all images of the same experiment.

Fluorescence intensity (FI) profiles in maximum intensity projection images of HCR stainings of colonies that were differentiated without stencils (Figure S8C) were measured in rectangular ROIs through the colony center. The spatial FI profiles were split at the center point between the colony edges which were determined based on SOX2 FI. The profiles for each colony half were averaged and normalized as described above.

T/BRA and SOX2 colocalization in differentiated cells

Thresholds for SOX2 and BRA fluorescence intensities were determined using Huang's fuzzy thresholding method in Fiji. Any pixels greater than or equal to this level were considered positive. Percentages were calculated as the proportion of pixels positive both SOX2 and BRA over all pixels positive for either SOX2 or BRA.

Fluorescence intensity profiles in embryos

Images of fluorescently labelled wholemounted embryos at E8.5 were analyzed in Fiji.[77] Measurements were obtained by tracing the edge of the SOX2$^+$ neural plate in maximum intensity projections using the freehand line tool with width set to 12 μm. FI profiles were obtained using the plot profile function. Profiles were smoothed using a rolling mean with a window size of 10. Profiles were normalized to the maximum value of each trace and background subtracted. For *Lmx1a* and BRA, background was defined as the minimum value of each profile. For pSMAD1/5 and *Nog*, the background was estimated using regions of the embryo that did not express these markers. To define the approximate position of the NMP region, we estimated the positions of the L1-L3 regions as described in Wymeersch et al.[78] in a subset of embryos. To this end, we estimated the position of the node from 3D z-stacks based on morphological appearance and the axial FI of *Lmx1a* and *Noggin* HCR. The L3 boundary position corresponds to 60 % of the length from the node to the posterior tip along the midline.

Biophysical model of BMP signaling dynamics

Specifying the reaction-diffusion system

The following section describes the derivation of the simplest reaction-diffusion network of BMP signaling dynamics that is consistent with experimental observations. The radial symmetry of the system allows the reaction-diffusion equations to be written only as a function of time and of the radial coordinate r. The system is simulated on a large domain $0 < r < R_\infty$. To account for the finite size of the colony, all production terms are non-zero only within the colony of radius R (by multiplying the production terms by the Heaviside function $\Theta(R - r)$), while diffusion and degradation can also take place outside the colony. The hypothesized interaction network for the ligand (BMP), BMP inhibitor (BMPi), phosphoSMAD1/5 (pSmad) and the transcription factor LMX1A (Lmx1a), whose concentrations are written as $\{b(r,t), i(r,t), s(r,t), l(r,t)\}$, is denoted as a set of partial differential equations. BMP and BMPi are diffusible species (with diffusion coefficients D_b and D_i).

The general set of equations used throughout are defined as:

$$\partial_t b = D_b \Delta_r b + P_b(s,l)\Theta(R - r) - d_b b \quad \text{(Equation 1)}$$

$$\partial_t i = D_i \Delta_r i + P_i(s)\Theta(R - r) - d_i i \quad \text{(Equation 2)}$$

$$\partial_t s = P_s(b,i)\Theta(R - r) - d_s s \quad \text{(Equation 3)}$$

$$\partial_t l = P_l(s,l)\Theta(R - r) - d_l l \quad \text{(Equation 4)}$$

where P_k and d_k are the production functions and degradation rates of species k. Since only the radial coordinate is modelled, only the r-derivatives of the polar coordinate Laplacian are used:

$$\Delta_r = \frac{\partial^2}{\partial r^2} + \frac{1}{r}\frac{\partial}{\partial r} \quad \text{(Equation 5)}$$

The dependencies of the production functions P_k are determined by the interactions in the reaction network outlined in Figures 4A and 4G. Throughout, this model is solved subject to the following boundary conditions:

$$\partial_r b(0,t) = 0 \quad \partial_r b(R_\infty, t) = 0 \quad \text{(Equation 6)}$$

$$\partial_r i(0,t) = 0 \quad \partial_r i(R_\infty, t) = 0 \quad \text{(Equation 7)}$$

using $R_\infty/R = 10$ for computational simplicity. Since the system is subjected to a spatially homogeneous exogenous BMP input at $t = 0$ with varying concentration denoted as b_0, the following initial condition for BMP is used:

$$b(r,0) = b_0 \quad \text{(Equation 8)}$$

The model suggests that the level of endogenously produced BMP far exceeds the exogenous BMP concentration, therefore the predicted dynamics are not sensitive to the addition of exogenous BMP every 24h (see sensitivity analysis below); for simplicity, exogenous BMP is implemented as b_0. In experiments, there is no expression of pSmad or Lmx1a at $t = 0$ (Figures 1D, 1F, 2A, and 2C).Therefore, the initial conditions are:

$$i(r,0) = s(r,0) = I(r,0) = 0 \quad \text{(Equation 9)}$$

Together, Equations 1, 2, 3, 4, 5, 6, 7, 8, and 9 fully specify the reaction-diffusion system.

Simplified model of the first phase dynamics

To gain insight into first phase pSmad dynamics, a reduced network is explored (Figures 4A and S4A). To reduce the number of parameters, the simplest implementation with linear reaction kinetics for BMP and BMPi, and a generic Hill function for pSmad activation arising from a balance of BMP and BMPi levels, is considered:

$$\partial_t b = D_b \Delta_r b + a_b^{(s)} s\Theta(R - r) - d_b b \quad \text{(Equation 10)}$$

$$\partial_t i = D_i \Delta_r i + a_i^{(s)} s\Theta(R - r) - d_i i \quad \text{(Equation 11)}$$

$$\partial_t s = \frac{b^h}{b^h + (i/K_i)^h}\Theta(R - r) - d_s s \quad \text{(Equation 12)}$$

where $a_n^{(m)}$ is the activation rate of species n by species m and K_i is the threshold at which pSmad production becomes sensitive to BMPi concentration.

Non-dimensionalization. To reduce the number of parameters in the model, equations are non-dimensionalized. The non-dimensionalization process for Equations 10, 11, and 12 is shown below. Equivalent steps are followed for the more complex models, for which only the non-dimensionalized equations are given.

For comparing the behavior of normalized concentrations, the dimensions of each species' concentration were removed. Furthermore, the dimensions of space were removed by normalizing the colony radius to $R = 1$, while keeping the time units in order to facilitate comparison of the timecourses to experiment. First, the non-dimensionalization constants c_m are defined for each species m:

$$r = R\tilde{r} \quad b = c_b\tilde{b} \quad i = c_i\tilde{i} \quad s = c_s\tilde{s} \quad \text{(Equation 13)}$$

These are substituted into Equations 10, 11, and 12:

$$\partial_t \tilde{b} = \frac{D_b}{R^2}\Delta_r \tilde{b} + \frac{a_b^{(s)} c_s}{c_b}\tilde{s}\Theta(1 - \tilde{r}) - d_b\tilde{b} \quad \text{(Equation 14)}$$

$$\partial_t \tilde{i} = \frac{D_i}{R^2}\Delta_r \tilde{i} + \frac{a_i^{(s)} c_s}{c_i}\tilde{s}\Theta(1 - \tilde{r}) - d_i\tilde{i} \quad \text{(Equation 15)}$$

$$\partial_t \tilde{s} = \frac{a_s^{(b)}}{c_s}\frac{b^h}{b^h + \left(\frac{c_i\tilde{i}}{c_b K_i}\right)^h}\Theta(1 - \tilde{r}) - d_s\tilde{s} \quad \text{(Equation 16)}$$

$\{c_b, c_i, c_s\}$ can be freely set such that three parameter combinations can be set to unity. Setting the prefactor of each concentration term to unity yields:

$$c_b = a_b^{(s)} a_s^{(b)} \quad c_i = a_i^{(s)} a_s^{(b)} \quad c_s = a_s^{(b)} \quad \text{(Equation 17)}$$

Thus, the non-dimensionalized versions of Equations 10, 11, and 12 are:

$$\partial_t \tilde{b} = \tilde{D}_b \Delta_r \tilde{b} + \tilde{s}\Theta(1 - \tilde{r}) - d_b\tilde{b} \quad \text{(Equation 18)}$$

$$\partial_t \tilde{i} = \tilde{D}_i \Delta_r \tilde{i} + \tilde{s}\Theta(1-\tilde{r}) - d_i \tilde{i} \quad \text{(Equation 19)}$$

$$\partial_t \tilde{s} = \frac{b^h}{b^h + (\tilde{i}/\tilde{K}_i)^h}\Theta(1-\tilde{r}) - d_s \tilde{s} \quad \text{(Equation 20)}$$

with $\tilde{D_m} = D_m/R^2$ and $\tilde{K_i} = a_b^{(s)} K_i / a_i^{(s)}$. Note that, if desired, time can be additionally be non-dimensionalized by setting $t = \tilde{t}/d_b$, giving time units of $1/d_b$. However, here, time is kept in units of hours for more intuitive comparison to experiments. Relabeling all variables to drop the tilde yields the non-dimensionalized equations used through the rest of the text:

$$\partial_t b = D_b \Delta_r b + s\Theta(R-r) - d_b b \quad \text{(Equation 21)}$$

$$\partial_t i = D_i \Delta_r i + s\Theta(R-r) - d_i i \quad \text{(Equation 22)}$$

$$\partial_t s = \frac{b^h}{b^h + (i/K_i)^h}\Theta(R-r) - d_s s \quad \text{(Equation 23)}$$

where $\Theta(R-r)$ was reintroduced for clarity and $R = 1$ is assumed throughout. Note that the consequences of changing reaction rates that have been removed in the process of non-dimensionalization can still be explored. For instance, the consequences of changing $a_b^{(s)}$, or model inhibitor knock-out models were explored by changing $a_i^{(s)}$. In this case, the corresponding reaction terms are simply rescaled by a dimensionless prefactor (see below).

Steady-state analysis of the first phase network. Based on the simulations of Equations 21, 22, and 23, the spatial profiles of pSmad have a near-constant length scale over time, consistent with experiments. Thus, the temporal dynamics of the circuit are captured by the maximum levels of pSmad signaling at every time point. These dynamics are approximately described by a set of ordinary differential equations for the concentrations at the colony edge, which allows the analytical solution for the steady-state concentrations as a function of the different model parameters:

$$\frac{db}{dt} = a_b^{(s)} s - d_b b \quad \text{(Equation 24)}$$

$$\frac{di}{dt} = s - d_i i \quad \text{(Equation 25)}$$

$$\frac{ds}{dt} = \frac{b^h}{b^h + (i/K_i)^h} - d_s s \quad \text{(Equation 26)}$$

In the experiments, the system is subjected to an initial exogenous BMP concentration to which it responds by pSmad activation and subsequent production of endogenous BMP and BMPi. Within the framework of the model, the temporal response of the system to the initial condition Equation 8 was characterized, and its subsequent approach to a steady state denoted by b^*.

$$b^* = \frac{a_b^{(s)}}{d_b} s^* \quad \text{(Equation 27)}$$

$$i^* = s^*/d_i \quad \text{(Equation 28)}$$

$$s^* = \frac{1}{d_s}\frac{\left(a_b^{(s)}/d_b\right)^h}{\left(a_b^{(s)}/d_b\right)^h + (1/(K_i d_i))^h} \quad \text{(Equation 29)}$$

The dependence of the steady-state concentrations as a function of parameters in Figures S4B–S4D show that there are three possible parameter regimes with different behaviors:

- Regime I: near-zero-steady state: $b^* \approx 0$. For very low BMP production $a_b^{(s)}$, the steady-state BMP concentration is nearly zero in this model.
- Regime II: non-zero steady state approached from below: $b_0 < b^*$. At larger values of BMP production $a_b^{(s)}$, the BMP steady state is non-zero and can be approached from below, i.e. the initial exogenous BMP concentration is lower than its steady-state value.
- Regime III: non-zero steady state approached from above: $b_0 > b^* > 0$. Alternatively, in the non-zero steady state regime, the initial condition may be larger than the steady state BMP concentration.

Simulations for the full spatio-temporal model (Equations 21, 22, and 30), indicate that the steady-states of this model are in agreement with the simplified analysis above (Figure S4E). Importantly, the timing of the pSmad maximum appears robust across these three regimes, as it is determined by the relative delay between BMP and BMPi concentrations (Figures S4E and S4G, inset). However, the three parameter regimes exhibit quantitatively different downregulation from the first phase peak as quantified in Figures 4C and S4F.

The parameters corresponding to regime III most closely agree with key experimental observations (rapid upregulation with strong subsequent downregulation of the first peak, pSmad concentration is finite at long times in the Lmx1a KO, no endogenous BMP production in the system at early timepoints).

Crucially, none of the three parameter regimes can result in oscillations in which the second peak has a similar amplitude as the first one, as observed in the experimental dynamics, even when additional parameters such as the inhibitor time-scale are varied (Figure S4H). Thus, additional species and interactions were considered to explain the experimental observations.

Modeling the edge activation of pSmad

This study aims to investigate the temporal dynamics of pSmad signaling, which, according to the model, is qualitatively unaffected by the specifics of the spatial dynamics. Nevertheless, possible implementations of the model that can account for the higher pSmad activation observed at the colony edge are considered.

Throughout the manuscript, the simple assumption that the boundary cells have increased sensitivity to BMP ligands is made, similar to what has been observed in previous work.[22] To incorporate the stronger activation of pSmad by BMP near the colony edge, Equation 23 is modified as follows:

$$\partial_t s = \frac{b^h}{b^h + (i/K_i)^h} \frac{1 + Af(r - R)}{1 + A} \Theta(R - r) - d_s s \qquad \text{(Equation 30)}$$

with $f(x) = \exp[-x^2/(2\sigma^2)]$. This model also captures an enhanced pSmad activation at the colony edge (Figure S5A).

To test this possibility from a theoretical perspective, the spatial profiles during the first phase of the dynamics are considered. When BMP and BMPi diffuse equally fast, their concentration profiles are predicted to peak at the colony center. This is because BMP and BMPi are produced within the colony, but are free to diffuse and degrade outwards (Figure S5B). In this scenario, pSmad activation occurs approximately uniformly throughout the colony, which is in contrast to the experimentally observed higher pSmad levels at the colony periphery. By contrast, the model indicates that when BMPi diffuses faster than BMP, this leads to a shallower gradient of BMPi at the edge compared to BMP. This causes locally enhanced pSmad activation at the edge, activating a positive feedback loop where consequently more BMP is produced locally, enhancing the edge effect (Figure S5B). This effect becomes more pronounced with increasing D_i/D_b (Figure S5B). This indicates that fast inhibitor diffusion leading to reduced inhibitor concentration at the colony edge is a plausible mechanism that could explain how pSmad activation at the edge arises.

To test this, colonies were cultured without removing the stencils, thus preventing lateral diffusion from the edge. In contrast to control colonies, exposure to BMP4 did not result in pSmad1/5 activation in these confined colonies (Figure S3B), which is consistent with an inhibitor diffusion model.

Next, assumptions on how the increased sensitivity of the edge cells arises in the system are tested. In the colonies, the activation of pSmad1/5 occurred beyond the first row of cells that are localized directly at the edge (Figures 2A, 2B, and 5F), suggesting that lateral receptor accessibility is not the main cause of the stronger response at the edge. Furthermore, the edge activation of pSmad1/5 also occurred in the presence of the ROCK inhibitor Y-27632 which reduces cortical tension (Figure S3A), arguing against a mechanical effect. An alternative possibility is that diffusion of a uniformly expressed BMP inhibitor away from the colony results in lower inhibitor concentrations and thereby higher activation of pSmad at the edge.

Expanded models including second phase dynamics

To capture the second phase of the experimental dynamics the possibility that Lmx1a, which was shown to activate BMP ligand production,[34,35] plays a key role in mediating the upregulation of pSmad in the second phase was explored (Equation 31). Furthermore, the observation that BMP signaling can promote Lmx1a expression is incorporated[11] (Equation 34). In the simplest approach, a model in which Lmx1a production is determined only by pSmad levels is explored:

$$\partial_t b = D_b \Delta_r b + \left[s + a_b^{(l)} l \right] \Theta(R - r) - b \qquad \text{(Equation 31)}$$

$$\partial_t i = D_i \Delta_r i + s\Theta(R - r) - d_i i \quad \text{(Equation 32)}$$

$$\partial_t s = \frac{b^h}{b^h + (i/K_i)^h}\Theta(R - r) - d_s s \quad \text{(Equation 33)}$$

$$\partial_t l = P_l(s)\Theta(R - r) - d_l l \quad \text{(Equation 34)}$$

Linear model of Lmx1a activation by pSmad. Modelling the simplest possibility of linear activation of Lmx1a by pSmad, $P_l(s) = s$ (with no rate parameter due to non-dimensionalization, see above) introduces two additional free fitting parameters: (1) the degradation rate of Lmx1a d_l, which determines the time-scale of its response; (2) the activation rate of BMP by Lmx1a $a_b^{(l)}$. These parameters were therefore varied to test whether this model can capture the experimental dynamics. At large Lmx1a time-scales $\tau_l = 1/d_l \gtrsim 20h$, this model captures the basic qualitative separation of the two phases of signaling, with a first pSmad peak, and a second phase with slowly increasing pSmad levels (Figure S6A). However, this model fails to quantitatively capture other features of the data: Lmx1a concentrations are predicted to rise gradually from $t = 0$, whereas in experiments, Lmx1a protein is not observed before 24h (Figures 1D and 1F). This is a fundamental limitation of this linear model: given that the maximal intensities of pSmad are similar in the first and second phases, a linear relation between pSmad and Lmx1a would always predict similar levels of Lmx1a production in the first and second phase, which is in contrast to the experimental observation. Therefore, next a potential nonlinearity in the Lmx1a dynamics was investigated to better capture the experimentally observed slow upregulation of Lmx1a and experimentally measured time-scale of Lmx1a degradation. To this end, the key time-scale parameter τ_l was inferred from experiments to constrain the model search as follows.

Inference of time-scale parameters from experimental data. To measure τ_l, the decay of Lmx1a levels was measured upon experimentally inhibiting protein production using cycloheximide at $T = 72h$. The decay dynamics indicate the degradation rate of the protein, corresponding to no further activation of Lmx1a in the model:

$$\partial_t l = -d_l l \rightarrow l(t - T) = l(T)e^{-d_l t} \quad \text{(Equation 35)}$$

Next, $\tau_s = 1/d_s$ was measured by experimentally inhibiting BMP signaling using the BMP receptor inhibitor LDN193189 at $T = 72h$, and monitoring the subsequent decay of pSmad levels. Since LDN disrupts all BMP signaling, this is equivalent to setting as to zero at $T = 72h$ in the model and monitoring the subsequent decay dynamics. These are then given by

$$\partial_t s = -d_s s \rightarrow s(t - T) = s(T)e^{-d_s t} \quad \text{(Equation 36)}$$

Based on exponential fits to the data as shown in Figure 4H, the following values were obtained

$$1/d_s \approx 0.63 \pm 0.04 \text{ h}, \quad \text{(Equation 37)}$$

$$1/d_l \approx 6.7 \pm 0.8 \text{ h}. \quad \text{(Equation 38)}$$

corresponding to half-lives $t_{1/2}^{(k)} = \ln(2)/d_k$:

$$t_{1/2}^{(s)} \approx 0.43 \pm 0.03 \text{ h}, \quad \text{(Equation 39)}$$

$$t_{1/2}^{(l)} \approx 4.7 \pm 0.5 \text{ h}. \quad \text{(Equation 40)}$$

for pSmad and Lmx1a, respectively. Thus, the intrinsic response time of pSmad is much faster than the experimentally observed pSmad upregulation in the second phase, indicating that the second phase upregulation reflects the dynamics of slower pathways that regulate pSmad. Furthermore, Lmx1a, despite having much slower timescale than pSmad, is faster than suggested by the simplified linear model of pSmad dependent regulation. Altogether, this suggests that the experimentally observed time scales are incompatible with a simple linear model of Lmx1a activation by pSmad.

Nonlinear model of Lmx1a activation by pSmad. Nonlinear activation of Lmx1a by pSmad alone was implemented as follows:

$$P_l(s) = \frac{s^h}{s^h + K_l^h}. \quad \text{(Equation 41)}$$

Given the measured Lmx1a degradation rate (Equation 38), this model is also unable to capture the pronounced two-phase behavior (Figure S6B). Specifically, for any parameter combination, Lmx1a responds early on during the first phase of the dynamics, due to its relatively fast response time-scale. As above, this is a generic issue with this model due to the fact that pSmad maximal

levels are similar during the first and second phase, leading to similar values of $P_l(s)$ in both phases even in a non-linear model. Thus, it is a generic feature of this model that the pSmad and Lmx1a dynamics will follow each other closely. Overall, given the measured degradation time-scales of pSmad and Lmx1a, a model of Lmx1a activation by pSmad alone is unable to capture the two-phase dynamics observed in experiments.

Expanded model with positive feedback on Lmx1a expression

Given the inability of both linear and non-linear models of Lmx1a activation by pSmad alone to accurately predict Lmx1a dynamics, the model was extended so that Lmx1a is weakly activated by pSmad with rate $a_l^{(s)}$, and in addition, engages in a positive feedback loop to promote its own production. This was implemented as (1) a self-activation of Lmx1a, (2) positive feedback by Wnt, so that Lmx1a activates Wnt, and Wnt activates Lmx1a. These two models are consistent with each other, demonstrating that the key aspect of the model is the presence of a positive feedback loop. The Wnt model is used throughout unless otherwise specified, while direct self-activation results are shown below.

Positive feedback through Lmx1a self-activation. Given the inability of the linear model to accurately predict Lmx1a dynamics, the self-activation of Lmx1a to promote its own production, while pSmad provides only a weak direct activation of Lmx1a with rate $a_l^{(s)}$, was considered. The self-activation of Lmx1a is captured by a Hill function, in which K_l is a non-linear threshold of self-activation:

$$\partial_t l = \left[a_l^{(s)} s + \frac{l^h}{K_l^h + l^h}\frac{s^h}{K_s^h + s^h}\right]\Theta(R - r) - d_l l. \quad \text{(Equation 42)}$$

In addition, a second Hill function dependent on pSmad was included, thus positing that the Lmx1a self-activation is pSmad-dependent. This is required to capture the decay of Lmx1a upon LDN treatment (Figure S7C), as it would otherwise continue to self-activate without decay. This additional Hill function does not otherwise strongly influence the model dynamics.

This model is the simplest implementation of non-linear dynamics which agrees with the LDN experiment, and adds two key parameters, $a_l^{(s)}$ and K_l. Varying both of these parameters recapitulates the experimentally observed dynamics in parameter regions where the weak activation of Lmx1a by pSmad crosses the threshold once the first phase peak has decayed (Figure S6C). This cue from pSmad into Lmx1a therefore ensures that the signal is relayed from the first to the second phase.

Positive feedback through Wnt. The experimental results suggest that Wnt signaling and Lmx1a positively regulate each other (Figure 4H), motivating a model where Wnt mediates the positive feedback on Lmx1a, such that Wnt activates Lmx1a and Lmx1a activates Wnt. Wnt is introduced as a diffusible species $w(r,t)$ as follows:

$$\partial_t l = \left[s + a_l^{(w)}\frac{w^h}{K_l^h + w^h}\frac{s^h}{K_s^h + s^h}\right]\Theta(R - r) - d_l l \quad \text{(Equation 43)}$$

$$\partial_t w = D_w \Delta_r w + l\Theta(R - r) - d_w w \quad \text{(Equation 44)}$$

Note that in Equation 43, a second Hill function dependent on pSmad was included, thus positing that the Lmx1a activation by Wnt is pSmad-dependent. As discussed above, this is required to capture the decay of Lmx1a upon LDN treatment (Figure 4C), as it would otherwise continue to self-activate without decay.

This model is the simplest implementation of a positive feedback loop on Lmx1a through a third species, hypothesized to be Wnt. Similar to the self-activation model, there are two additional key parameter $a_l^{(w)}$ and K_l that determine the dynamics (Figure S6D). For ease of interpretation, the parameter $a_l^{(s)}$ is systematically varied, which is equivalent to varying $a_l^{(w)}$ and other associated Lmx1a parameters. This model predicts upregulation of endogenous Wnt in the second phase, engaging in a positive feedback loop with Lmx1a (Figure S9A). Note that Figure S8C indicates that Wnt activity (Axin2) is high also at the beginning of the timecourse - this effect results from the preceding step of the differentiation protocol in which the Wnt pathway is transiently activated using CHIR. Unless otherwise mentioned, this model is used in all main and supplementary figures.

Sensitivity analysis of the model

This section outlines how sensitive the model is to various assumptions and parameter choices. First, the sensitivity of the dynamics to the continuous presence of exogenous BMP in the medium is tested by implementing a constant background production rate a_0:

$$\partial_t b = D_b \Delta_r b + a_0 + \left[s + a_b^{(l)} l\right]\Theta(R - r) - b. \quad \text{(Equation 45)}$$

In the experiments, exogenous BMP corresponding to the initial concentration b_0 is resupplied every 24h, therefore $a_0 = b_0/24h^{-1}$. Simulations indicate that the changes to the dynamics are minimal, even for a two-fold higher background rate (Figure S9B). This is the case, because the BMP produced in the model (corresponding to endogenously produced BMP in the default model without a_0) far exceeds the effective concentration of exogenous BMP, represented by b_0 (by a factor of $\approx$40 for the lowest exogenous BMP concentration). Thus, the dynamics is dominated by the endogenous, rather than exogenous BMP. Differences in the effective concentrations of exogenous and endogenous BMP could result from multiple factors influencing the ability of these ligands to spread and signal, such as post-translational modifications, dimer formation and others. Furthermore, the model captures a single generic BMP ligand, while cells produce several BMP ligands (Figure S2C) which may have cooperative activities.[79]

Second, the sensitivity of the predicted timecourse to the value of the diffusion coefficients is tested. For simplicity, all diffusion coefficients are set to be equal, $D_b = D_i = D_w = D$. The same qualitative dynamics independent of the magnitude of the diffusion coefficients was observed, although lower diffusion coefficients lead to a smaller delay in the onset of the second phase (Figure S9C). More pronounced differences are observed when the diffusion coefficients of BMP and BMPi are not equal (see below).

Model predictions

Varying exogenous BMP concentration. A key prediction of the model is its behavior as a function of varying exogenous BMP (exBMP) concentration. Experimentally, the response to the following set of concentrations is tested: { 0.5,1.5,3,5 } ng/ml. To model the varying exBMP concentrations, the following set of initial conditions are used:

$$b(r, t = 0) = \{b_0, 3b_0, 6b_0, 10b_0\}, \quad \text{(Equation 46)}$$

which represents the same relative increase in concentration as in the experiment. The amplitudes of the pSmad peak and minimum levels in the first phase increase with exBMP concentration (Figures 5H, S11A, and S11C). This increase exhibits a saturating trend well predicted by the model due to the nonlinearity in the pSmad inhibition (Equation 30), which implies a maximum rate of pSmad production. The peak amplitude of key BMP inhibitors, including Noggin, exhibit a similar increasing trend with exBMP, as observed experimentally in RNAseq (Figures S3C and S11B). In contrast, the model predicts that the duration of the first phase – defined as the time elapsed between the first maximum and the minimum of pSmad concentration – is nearly constant as the exBMP concentration is increased tenfold (Figures S11C and S11D). Specifically, the duration decreases by only ≈15%, while the amplitude increases by ≈60%.

BMP inhibitor knockouts. To test the role of the BMP inhibitor species, a condition in which the production of the BMP inhibitor is reduced was simulated (Figure S11E). A reduction by 30% for the Noggin knockout experiment corresponds to setting $a_i^{(s)} = 0.7$ (as defined in Equation 11), compared to its standard value in the non-dimensionalized set of equations of $a_i^{(s)} = 1$. Because several inhibitors of BMP are expressed upon BMP treatment in cultured cells (including Noggin, Smad6/7, Figure S3), this simple model allows to predict how knocking out one of these inhibitors impacts the dynamics of the system.

Temporal behaviors predicted by the model. Phase diagrams of the typical pSmad and Lmx1a temporal dynamics as a function of key parameter combinations were generated to explore the possible behaviors predicted by the model.

Specifically, behaviors as a function of BMP and Lmx1a activation rates by pSmad, $a_b^{(s)}$ and $a_l^{(s)}$, respectively, are explored (Figure S12A). To distinguish different classes of behaviors, two key aspects of the dynamics were quantified. To measure the downregulation of pSmad after the first phase, the fractional downregulation $D = 1 - s_{\min}/s_{\max}$, where $s_{\max}$ is the maximum pSmad amplitude in the first phase, and $s_{\min}$ is the amplitude of the subsequent minimum (Figure S12B), was defined. This definition is used to quantify the degree of downregulation on a unique scale from 0 to 1. Since $s_{\min} < s_{\max}$ by definition, and thus $0 < s_{\min}/s_{\max} < 1$, and therefore D is between 0 and 1, with $D = 1$ if $s_{min} = 0$ (complete downregulation) and $D = 1$ if $s_{\min} = s_{\max}$ (no downregulation).

To measure the produced amount of Lmx1a, the Lmx1a concentration at the final timepoint, $I_{\text{final}} = I(t = 96)$, is recorded (Figure S12C). Based on these two quantities, three typical behaviors are observed (Figure S12A–S12C):

- first phase only: if the production rates are too low, the system fails to activate the Lmx1a self-activation loop, leading to failure of the relay mechanism (bottom left corner). In the phase diagram Figure 4J, this phase is defined wherever $I_{\text{final}} \approx 0$.
- simultaneous phases: if the production rates are too high, Lmx1a self-activates before pSmad was downregulated significantly, leading to no clear separation between first and second phase (top right corner). In the phase diagram Figure 4J, this phase is defined wherever pSmad is downregulated by less than 50% of its maximum amplitude, $D < 0.5$.
- temporal relay: between these two phases, we observe a broad parameter regime where a temporal relay with clear ordering of phases, significant pSmad downregulation, and subsequent activation of Lmx1a is observed.

Similarly, the behaviors as a function of the BMP activation rates by pSmad, $a_b^{(s)}$, and the initial exogenous BMP concentration b_0 were investigated (Figure S12D). In addition, the downregulation of pSmad and final amplitude of Lmx1a were quantified (Figures S12E and S12F). Similar qualitative behaviors as in Figures S12A–S12C were observed. Star symbols indicate the BMP concentrations in the model for varying exogenous BMP concentration, which are in a regime where the temporal relay behavior is robust to changes in the exogenous BMP concentration. Importantly, all parameter scans are performed in log-scale, meaning that each parameter regime is robust for a broad range of parameters.

Parameter overview

The parameter scans described above constrain the parameters of the model, which are summarized in Table S1. Here, non-dimensionalized parameters are shown. To provide re-dimensionalized values of the diffusion coefficients for comparison to literature values, the following relation is used:

$$D^{\text{dim}} = D^{\text{nondim}} R^2 = 0.001 \times (5 \times 300)^2\ \mu\text{m}^2\text{h}^{-1} = 0.6\ \mu\text{m}^2\text{s}^{-1} \quad \text{(Equation 47)}$$

with a final colony radius of ≈5 × 300 μm. This value is within the same order of magnitude of previously measured values of BMP diffusion coefficients. The range of these estimates is rather broad across different systems, ranging from Dpp in fly (0.1 $\mu\text{m}^2\text{s}^{-1}$[80]) to BMP in zebrafish (1 $\mu\text{m}^2\text{s}^{-1}$[81,82]). Importantly, the exact values of the diffusion coefficients do not strongly affect the predicted timecourse (see sensitivity analysis above).

Numerical implementation

The code used for model simulations is developed in Python 3 and is available at github (https://github.com/dbrueckner/NeuralTubeColonies, https://doi.org/10.5281/zenodo.13335390). The reaction-diffusion partial differential equations (PDE) are numerically integrated using NumPy.[83] All simulations are sped up by just-in time-compiling using numba jit. Specifically, the time derivative is approximated using Euler forward differences, and the spatial derivative using centered differences. The PDE is simulated on a one-dimensional domain $[0, R_\infty]$. The following scheme for each species' concentration $c_k(x,t)$ is used:

$$c_k(r, t+\delta t) = c_k(r,t) + [D_k g_{\text{diff}} c_k(r,t) + P_k(c_k(r,t), \{c_{j\neq k}\}) - d_i c_k(r,t)]\delta t \quad \text{(Equation 48)}$$

Here, g_{diff} is the operator for the second spatial derivative in polar coordinates, whose discrete form depends on the boundary conditions. Closed (von Neumann) boundary conditions are used, enforcing vanishing flux at the boundaries, i.e.,

$$\frac{\partial c_k(r,t)}{\partial t}(0,t) = \frac{\partial c_k(r,t)}{\partial t}(R_\infty, t) = 0 \quad \text{(Equation 49)}$$

Using these boundary conditions:

$$g_{diff} = \begin{cases} \frac{c_k(r+\delta r,t) - 2c_k(r,t) + c_k(r-\delta r,t)}{\delta r^2} + \frac{1}{r}\frac{c_k(r+\delta r,t) - c_k(r-\delta r,t)}{2\delta r} \\ \frac{2c_k(r+\delta r,t) - 2c_k(r,t)}{\delta r^2} \\ \frac{-2c_k(r,t) + 2c_k(r-\delta r,t)}{\delta r^2} \end{cases} \quad \text{(Equation 50)}$$

is obtained.

To ensure sufficient spatial resolution of the profiles, δr is chosen to always be smaller than the smallest length-scale in the system:

$$\delta r = \min[1, 0.2 \times \min[\{l_k\}]] \quad \text{(Equation 51)}$$

where $l_k = \sqrt{D_k/d_k}$ are the length-scales of the diffusive species. To ensure numerical stability, a parameter-adapted time interval δt that satisfies the Courant- Friedrichs-Levy (CFL) criterion,[84,85] is used. Specifically, the CFL criterion states that the time interval should be smaller than a critical value

$$\delta t_{\text{CFL}^{(k)}} = \frac{2\delta r^2}{4D_k + d_k \delta r^2} \quad \text{(Equation 52)}$$

where D_k and d_k are the diffusion constant and decay rate of each species k. The criterion for all species was evaluated and the time interval chosen according to

$$\delta t = 0.2 \times \min\left[\delta t_{CFL}^{(k)}\right] \quad \text{(Equation 53)}$$